
Title: Rare earth and transition metal based entropy stabilised perovskite type oxides

Authors: Abhishek Sarkar, Ruzica Djenadic, Di Wang, Christina Hein, Ralf Kautenburger, Oliver Clemens, Horst Hahn

PII: S0955-2219(17)30867-1
DOI: https://doi.org/10.1016/j.jeurceramsoc.2017.12.058
Reference: JECS 11663

To appear in: *Journal of the European Ceramic Society*

Received date: 18-11-2017
Revised date: 22-12-2017
Accepted date: 26-12-2017

Please cite this article as: Sarkar A, Djenadic R, Wang D, Hein C, Kautenburger R, Clemens O, Hahn H, Rare earth and transition metal based entropy stabilised perovskite type oxides, *Journal of The European Ceramic Society* (2010), https://doi.org/10.1016/j.jeurceramsoc.2017.12.058

# Rare earth and transition metal based entropy stabilised perovskite type oxides

*Abhishek Sarkar,*[*,a,b] Ruzica Djenadic,[b,c,†] Di Wang,[a,d] Christina Hein,[e] Ralf Kautenburger,[e] Oliver Clemens,*[a,f] and Horst Hahn,*[a,b,c]*

[a]Institute of Nanotechnology, Karlsruhe Institute of Technology, Hermann-von-Helmholtz-Platz 1, 76344 Eggenstein-Leopoldshafen, Germany

[b]Joint Research Laboratory Nanomaterials – Technische Universität Darmstadt and Karlsruhe Institute of Technology, Alarich-Weiss-Str. 2, 64287 Darmstadt, Germany

[c]Helmholtz Institute Ulm – Electrochemical Energy Storage, Helmholtzstr. 11, 89081 Ulm, Germany

[d]Karlsruhe Nano Micro Facility, Karlsruhe Institute of Technology, Hermann-von-Helmholtz-Platz 1, 76344 Eggenstein-Leopoldshafen, Germany

[e]WASTe Group, Inorganic Chemistry, Saarland University, Campus Dudweiler, Am Markt Zeile 5, D-66125 Saarbrücken, Germany

[f]Materials Design by Synthesis Group, Technische Universität Darmstadt, Alarich-Weiss-Str. 2, 64287 Darmstadt, Germany

*Corresponding author: abhishek.sarkar@kit.edu, oliver.clemens@nano.tu-darmstadt.de, horst.hahn@kit.edu.

[†](R.D.) Heraeus Deutschland GmbH & Co. KG, Heraeusstr. 12 – 14, 63450 Hanau, Germany.

**ABSTRACT:**

Multicomponent oxides with perovskite type of structure containing up to 10 different cations in equiatomic amounts have been synthesised for the first time. Out of eleven systems synthesised, only six systems crystallised as single phase perovskite type compounds with random and homogenous cation distribution on the respective sites. The formation of phase pure 10-cationic system, $(Gd_{0.2}La_{0.2}Nd_{0.2}Sm_{0.2}Y_{0.2})(Co_{0.2}Cr_{0.2}Fe_{0.2}Mn_{0.2}Ni_{0.2})O_3$, in contrast to the multiphase mixtures observed in five of the lower entropy systems (containing 6 cations) indicates a possible role of entropy in the stabilisation of a single phase crystal structure. The entropy driven structural stabilisation effect is further supported by the reversible phase transformation, from single phase to multiple phase upon cyclic heat treatment, observed in the $(Gd_{0.2}La_{0.2}Nd_{0.2}Sm_{0.2}Y_{0.2})MnO_3$ system. This type of entropic signature has been observed in rocksalt based multicomponent equiatomic oxide systems. However, it has not been reported before for perovskite based compounds, as shown in this study.

**Keywords:** Spray pyrolysis; multicomponent equiatomic perovskites; high entropy oxides; structural distortion

## 1. INTRODUCTION

The discovery of new materials with advanced properties is one of the greatest challenges faced by the scientific community. Research work on high entropy materials was recently extended to oxide systems by Rost *et al.* [1], where it was observed that high configurational entropy can be effectively used to stabilise single phase rocksalt type systems containing five different cations in equiatomic amount. As per Murty *et al*. [2], a system can be classified as a high entropy material, if the configurational entropy ($\Delta S_{config}$) of that system is higher than 1.5R (0.0124 $kJ \cdot mol^{-1} \cdot K^{-1}$). In case of an oxide systems with cations sharing only one Wyckoff site (like in rocksalt based systems), the $\Delta S_{config}$ can only be greater than 1.5R if 5 (or more) cations are present in near equiatomic ratios. Furthermore, $\Delta S_{config}$ attains a maximum value when all the different elements are present in equiatomic amount. Although, the chemical bonding in the oxides are very different from the metallic bonds present in high entropy alloys (HEAs) [2,3], the presence of high configurational entropy (1.61R) found in the rocksalt based multicomponent oxide system ($(Co_{0.2}Cu_{0.2}Mg_{0.2}Ni_{0.2}Zn_{0.2})O$) [1] cannot be ignored. Additionally, the fact that this system shows a reversible transformation from a multiple phases (at lower temperature) to single phase (at higher temperature) upon cyclic heat treatment confirms the claim that the single phase structure in complex oxides can indeed be stabilised by enhancing the configurational entropy of the system [1,4]. This research on high entropy oxides (HEOs) [1] has opened up a new way to design complex multicomponent oxide ceramics. The functional properties of these new oxides are yet to be fully explored, but the initial studies by Bérardan *et al.* [5,6] show interesting and improved properties compared to binary or doped oxide systems, providing further motivation for extensive research in this field.

The field of high entropy oxides was further broadened by the discovery of multicomponent equiatomic rare earth oxides (ME-REOs) [7,8], where it has been shown that up to seven rare earth cations could be successfully incorporated into a phase pure fluorite type crystal lattice. Recently, Jiang *et al.* [9] observed that entropy stabilisation in oxides can be extended to complex systems like perovskites ($ABO_3$), where cations share two or more Wyckoff sites. The tendency to form secondary phase(s) on addition of more cations (in higher amounts than doping) could be expected to be higher for complex oxides like perovskites ($ABX_3$) than for oxides with simpler structure like rocksalt (AX) since the formation of other structures (e.g.,

ilmenite type) and/or phases of the type $A_xB_yX_z$ (e. g. Ruddlesdon-Popper type phases) are often alternatives in systems of higher chemical complexity. In the study by Jiang *et al.* [9] only the B-site was substituted by five different elements, whereas the A-site was fixed to one or at most two elements. Hence, in this study more complex perovskites with completely different compositions are studied, where both cation sites are populated with five different elements in equiatomic amounts, i.e., five on the A-site, or the B-site, and finally five on both the A-site and the B-site, forming a 10 equiatomic cationic system.

## 2. EXPERIMENTAL SECTION

**2.1. Cations selection.** Considering $ABO_3$ type system, three sets of multicomponent equiatomic perovskite oxide (ME-PO) systems were selected: (i) systems where the A-site was substituted with 5 rare earth cations in equiatomic amounts ($5A_{0.2}$ = $Gd_{0.2}La_{0.2}Nd_{0.2}Sm_{0.2}Y_{0.2}$), whereas the B-site was kept occupied with a single transition metal cation (Co, Cr, Fe, Mn, or Ni) forming five systems: $(5A_{0.2})CoO_3$, $(5A_{0.2})CrO_3$, $(5A_{0.2})FeO_3$, $(5A_{0.2})MnO_3$ and $(5A_{0.2})NiO_3$; (ii) systems where the B-site was substituted with 5 transition metal elements in equiatomic amounts ($5B_{0.2}$ = $Co_{0.2}Cr_{0.2}Fe_{0.2}Mn_{0.2}Ni_{0.2}$) and keeping the A-site occupied with a single rare earth cation (Gd, La, Nd, Sm, or Y) forming five systems: $(Gd(5B_{0.2})O_3$, $La(5B_{0.2})O_3$, $Sm(5B_{0.2})O_3$, $Nd(5B_{0.2})O_3$ and $Y(5B_{0.2})O_3$); and (iii) a system where both the A- and B-sites were replaced by 5 rare earth and 5 transition metal elements, respectively, in equiatomic amounts, forming 10-cationic $(Gd_{0.2}La_{0.2}Nd_{0.2}Sm_{0.2}Y_{0.2})(Co_{0.2}Cr_{0.2}Fe_{0.2}Mn_{0.2}Ni_{0.2})O_3$ system or in an abbreviated form $(5A_{0.2})(5B_{0.2})O_3$. The cations were chosen following criteria already reported for other HEOs [1,7], i.e., (i) the ionic radii of the cations (on a specific site, A or B) at a specific oxidation state and coordination number should be similar, and (ii) at least one of the perovskite systems should have different prototype structure (e.g. $YMnO_3$) [10]. An overview of the ionic radii and the space groups of various structures that could be formed using the selected elements are given in the Supplementary Information, Table S1 and S2, respectively.

**2.2. Synthesis.** ME-POs powders were synthesised using nebulised spray pyrolysis (NSP) [11]. The illustration of the experimental setup can be found elsewhere [12]. The nitrate salts of Gd, La, Nd, Sm, Y Co, Cr, Fe, Mn and Ni ($Gd(NO_3)_3{\cdot}6H_2O$, Sigma Aldrich, 99.9%; $La(NO_3)_3{\cdot}6H_2O$,

Sigma Aldrich, 99.9%; $Nd(NO_3)_3 \cdot 6H_2O$, Sigma Aldrich, 99.9%; $Sm(NO_3)_3 \cdot 6H_2O$, ABCR, 99.9%; $Y(NO_3)_3 \cdot 6H_2O$, ABCR, 99.9%; $Co(NO_3)_2 \cdot 6H_2O$, Sigma Aldrich, 99.9%; $Cr(NO_3)_3 \cdot 9H_2O$, Sigma Aldrich, 99.9%; $Fe(NO_3)_3 \cdot 9H_2O$, Sigma Aldrich, 99.9%; $Mn(NO_3)_2 \cdot 4H_2O$, ChemPure, 98.5%; $Ni(NO_3)_2 \cdot 6H_2O$, Sigma Aldrich, 99.9%) were used as precursors. A water-based solution containing appropriate equiatomic cation combinations (0.1 $mol \cdot L^{-1}$) was continuously delivered (~ 0.12 $L \cdot h^{-1}$) into the piezo-driven nebuliser. The generated mist containing fine droplets of the precursor solution was transported by flowing oxygen (5 standard $L \cdot min^{-1}$) into the hot-wall reactor where the particles were formed at a temperature of 1050 °C and a pressure of 900 mbar. The as-synthesised particles were collected using a filter-based collector and calcined at 1200 °C for 2 hours in air atmosphere with a heating/cooling rate of 10 $°C \cdot min^{-1}$.

**2.3. Characterisation.** The microstructure and elemental composition of the synthesised powders were studied using a Philips XL30 FEG scanning electron microscope (SEM) equipped with an energy dispersive spectroscopy (EDS) system (Amatek, USA). Particle size distribution was obtained by measuring around 300 particles and the average particle size was obtained from a log-normal fit [13].

For the validation of the elemental composition of the powders, selected samples have been analysed in triplicate by inductively coupled plasma mass spectrometry (ICP-MS) using an Agilent 7500cx ICP-MS (Agilent, Santa Clara, USA); detailed analytical conditions are given in the Supplementary Information (Table S3). For the measurements 10 mg of the synthesised powders were first dissolved in 2 ml $HNO_3$ (supra quality, 68%, Carl Roth, Karlsruhe, Germany) and 8 ml MilliQ deionised water (18.2 $m\Omega \cdot cm$). In a second step, 10 µL of the sample solution was further diluted with 9.68 mL MilliQ-water. Additionally, 10 µL of internal standard (10 $mg \cdot L^{-1}$ scandium and holmium, respectively) was added to correct the time dependent sensitivity variation of the ICP-MS system followed by an addition of 300 µL of nitric acid (68%, supra quality) to prohibit metal ion sorption onto the tube surface. For quantification a calibration with 0, 5, 25, 100 and 500 $\mu g \cdot L^{-1}$ of all analysed elements were prepared under similar conditions.

Room temperature X-ray diffraction (XRD) patterns of the powders were recorded using a Bruker D8 diffractometer with Bragg-Brentano geometry using Cu-Kα radiation with a Ni filter and a VANTEC detector having a fixed divergence slit (0.3°). A step size of 0.015° and a collection time of 4 s per step at 30 kV and 40 mA over the diffraction angle ($2\theta$) range between

10 and 90° were used. For in-situ high-temperature XRD (HT-XRD) measurements a temperature stage (Anton Paar HTK 1200, Bruker) was used to collect data in a temperature range between 30 °C and 1000 °C with a heating and cooling rate of 30 °C·min$^{-1}$. The step size and collection time were set to 0.015° and 2 s, respectively. Rietveld analysis (TOPAS 5, Bruker) [14] of the XRD patterns was performed to determine the structure and phase composition of powders. Perovskites phases could be refined using a standard orthorhombic perovskite type structure of $GdFeO_3$ (*Pbmn*, ICSD 23823). The structural files were modified according to the number and the type of elements present in the refined system. The instrumental intensity distribution for the XRD data was determined using a reference scan of $LaB_6$ (NIST 660a). Thermal displacement parameters were constrained to be the same for all atoms.

The TEM specimen was prepared by directly dispersing the powders onto a gold grid coated with holey carbon film. It was examined with a FEI Titan 80 – 300 electron microscope (FEI, Eindhoven, the Netherlands) equipped with CEOS image spherical aberration corrector, Fischione model 3000 high angle annular dark field (HAADF) scanning transmission electron microscopy (STEM) detector, EDAX SUTW energy dispersive X-ray spectroscopy (EDX) detector and Gatan Tridiem image filter. The microscope was operated at an accelerating voltage of 300 kV in TEM mode for HRTEM and in nanoprobe mode for STEM imaging, EDX and electron energy loss spectroscopy (EELS) spectra acquisition.

## 3. RESULTS AND DISCUSSION

**3.1. Microstructure and chemical composition**. The as-synthesised as well as the calcined multicomponent equiatomic perovskite based oxide (ME-PO) powders are mostly black in colour except for $(5A_{0.2})CrO_3$, $(5A_{0.2})FeO_3$, and $(5A_{0.2})NiO_3$, which are light green, brown and olive green, respectively (Figure 1a). The morphology of the calcined powders studied by SEM (Figure 1b) show spherical hollow agglomerates of particles having a mean particle size of 180 nm (inset in Figure 1b).

The actual compositions of the systems could be the determined for 5 of the 11 compounds by ICP-MS (Supplementary Information Table S4). The other 6 compounds could not be dissolved completely in a concentrated acid. The obtained overall compositions confirm that all the elements in those 5 ME-POs are present in the desired stoichiometry. The EDS analysis (see Supplementary Information Table S5) performed on the systems are in good agreement with the

ICP-MS results, which confirm the correct overall compositions for the systems which could not be analysed using ICP-MS.

**3.2. Phase composition and structural analysis.** The XRD patterns of the as-synthesised powders, Supplementary Information Figure S1 (a-d), show that only one of the ME-PO systems, $(5A_{0.2})CoO_3$, completely crystallises as a single phase solid solution directly under the synthesis conditions used, whereas in some of the systems ($(5A_{0.2})CrO_3$, $(5A_{0.2})FeO_3$, $La(5B_{0.2})O_3$, $Nd(5B_{0.2})O_3$) several phases are formed. In all the other systems ($(5A_{0.2})MnO_3$, $(5A_{0.2})NiO_3$, $Gd(5B_{0.2})O_3$, $Y(5B_{0.2})O_3$ and $(5A_{0.2})(5B_{0.2})O_3$) a large amount of amorphous phase is observed. One of the reasons for the presence of more than one phase in some of the systems and incomplete crystallisation in the others can be the low residence time (around 150 ms) of the particles in the NSP reactor. The residence time plays an important role in diffusion and crystallisation processes. Hence, all as-synthesised powders were subjected to a further calcination step at 1200 °C for 2 hours in air and only the calcined powder are used for further characterisation and discussion. The corresponding XRD patterns are shown in Figure 2 (a-d) and the summary of their detailed structural analysis are given in Table 1.

The Rietveld analysis shows that all of the systems except $(5A_{0.2})NiO_3$ crystallise in orthorhombic perovskite type structure, but with different structural parameters and degree of secondary phases. The Rietveld refinements of all the systems (along with the Bragg peak position of the secondary phases for the multiphase mixtures) are provided in the Supplementary Information (Figure S2-S11). The average crystallite size of the perovskite phases for the different ME-POs ranges from 75–125 nm where $(5A_{0.2})CoO_3$ has the smallest and $Sm(5B_{0.2})O_3$ has the largest crystallite size. Minor amount of non-perovskite phases (up to a maximum of 5 wt.%) are observed in three of the systems: $(5A_{0.2})CrO_3$, $Sm(5B_{0.2})O_3$ and $Y(5B_{0.2})O_3$.

In the $(5A_{0.2})MnO_3$ system no additional non-perovskite type phases are found. However, strong tails at lower diffraction angles are observed for all the reflections in the XRD pattern for this system. The pattern of this phase cannot be refined using a single perovskite type phase, which is seen by the misfit (Figure 3a) of the (020) reflection at 31.1° (2θ). This reflection shows a misfit

due to its strong asymmetry, which indicates a distribution of perovskites phases with similar lattice parameters, mutually resulting from a non-isotropic composition. Therefore, the flexibility of the model needs to be increased to describe the observed pattern, and it was found that a series of three orthorhombic perovskite phases with very close lattice parameters (same shape and positional parameters for all perovskite phases, see Table 1) can be used to approximately model the pattern (Figure 3b). For this 3-phase model an increase of the *a*-axis with decrease of the *b*- and *c*-axes for the different phase fractions was found. The fit can be further improved by choosing a smoother distribution of *n* perovskite phases, by adding a constraint in such a way that the lattice parameters $(a,b,c)_i$ of phase fraction *i* are calculated according to :

$$(a,b,c)_i = (a,b,c)_{i=1} + [(a,b,c)_{i=n} - (a,b,c)_{i=1}] * (i/n) \quad (1)$$

in addition to constraining the phases to the same shape and positional parameters (i.e., independent of the number of *n*, only 6 lattice parameters, $(a,b,c)_{i=1}$ and $(a,b,c)_{i=n}$, are being refined, which mimics the width of the distribution of the phases, with additional *n* scaling parameters). The phase distribution model for a fit with $n = 8$ is given in the Supplementary Information, Table S6. Again, this agrees well with a segregation of rare earth cations based on their size. Figure 3(a-c) compares Rietveld fits of the $(5A_{0.2})MnO_3$ XRD pattern by either considering a single perovskite (a) or three perovskite (b) or an $n = 8$ perovskite phases (c). In the $(5A_{0.2})NiO_3$ system, a major monoclinic phase ($Gd_2O_3$ type) instead of an orthorhombic perovskite phase, with higher amount of secondary rocksalt (NiO type) and tetragonal ($La_2NiO_4$ type) phases, are observed. The major $Gd_2O_3$ type phase is most likely a solid solution containing several of the rare earth cations in it.

From the XRD patterns (Figure 2a-c), it can be clearly observed ($2\theta = 20°–30°$) that the intensities of the superstructure reflections varies in different ME-POs. This intensity variation is strongly dependent on the degree of deviation from the cubic perovskite structure, which indeed strongly depends on the lattice parameters (Table 1) of the perovskite phases. The pictorial representation of distortion from the ideal cubic lattice, based on the structural information obtained from Rietveld refinement, is shown in the Supplementary Information (Figure S12 (a) and (b)). The Goldschmidt's tolerance factor (*t*) is a well-known theoretical parameter used for explaining this type of deviation from cubic symmetry and is calculated from the ionic radii [15] based on the following equation [16]:

$$t = \frac{r_A + r_O}{\sqrt{2}(r_B + r_O)} \quad (2)$$

where $r_A$ and $r_B$ are the ionic radii of the cation at A-site and B-site (see Table S1 in the Supplementary Information), respectively, and $r_o$ is the radius of the oxygen ion. In case of multiple cations at a specific site an average of the ionic radii is considered.

In an ideal case, for the cubic structure *t* should be equal to 1. For $t < 1$, i.e., for systems with smaller A-site cation or bigger B-site cations, orthorhombic or rhombohedral structures are preferred, whereas tetragonal or hexagonal structures are preferably formed for $t > 1$. In case of ME-POs orthorhombic perovskite phases are observed as the value of *t* is lower than 1 (Table 2) and the deviation from the cubic symmetry becomes more prominent with adding (or substituting smaller cation) on the A-site or bigger on the B-site. Another parameter which is often used to explain the deviation from the pseudo-cubic symmetry is the degree of metric distortion ($\varepsilon$) which can be defined as [17]:

$$\varepsilon = \left(\frac{1}{3}\right) \cdot \left[\left\{\frac{a_{norm} - a_{ps.cubic}}{a_{ps.cubic}}\right\}^2 + \left\{\frac{b_{norm} - a_{ps.cubic}}{a_{ps.cubic}}\right\}^2 + \left\{\frac{c_{norm} - a_{ps.cubic}}{a_{ps.cubic}}\right\}^2\right]^{0.5} \quad (3)$$

where $a_{ps.cubic}$ is the pseudo-cubic lattice parameter, and $a_{norm}$, $b_{norm}$, $c_{norm}$ are the normalised values of pseudo-cubic lattice parameters taking into account the orientation of the lower symmetry cell. These values are calculated from the following equations:

$$a_{ps.cubic} = \sqrt[3]{V} \quad (4)$$

$$a_{norm} = \frac{a}{\sqrt{2} \cdot \sqrt[3]{V}}, \; b_{norm} = \frac{b}{\sqrt{2} \cdot \sqrt[3]{V}}, \; c_{norm} = \frac{c}{2 \cdot \sqrt[3]{V}} \quad (5)$$

where *V* is the volume per $ABO_3$ unit, i.e.,

$$V = \frac{a * b * c}{4} \quad (6)$$

with *a, b, c* being the original lattice parameter of the orthorhombic (*Pbnm*) perovskites obtained from the Rietveld analysis (Table 1). In case of $\varepsilon$, the extent of deviation from the ideality follows a similar trend as the theoretical parameter *t* (Table 2). With decrease in the cationic radii at the A-site, or increase in the cationic radii at the B-site (see Table S2 for the ionic radii of the cations given in the Supplementary Information), $\varepsilon$ deviates strongly from ideality ($\varepsilon > 0$) and

hence, a lowering in degree of symmetry or a higher magnitude of distortion is observed. The tilting and distortion of the $BO_6$ octahedra in the perovskite oxides is known to be the genesis of several of their important functional properties like magnetic, ferroelectric, etc. [18]. The distortion in perovskite structure from the ideal cubic symmetry is strongly governed by the shape or relative orientation of these $BO_6$ polyhedra [19]. There can be three different cases: (i) cations displacement inside the octahedra mostly observed for smaller B-cations (often leading to polar structures), (ii) tilting of the octahedra mostly observed for smaller A-cations which are too small to be accommodated within a cuboctahedral cage site (often leading to orthorhombic or rhombohedral structures), and (iii) distortion of the $BO_6$ polyhedra often seen for compounds with Jahn-Teller active cations (e.g., $Cu^{2+}$, $Mn^{3+}$) [18,20]. Figure S12(c-e) in the Supplementary Information illustrates the increasing tilt of the $BO_6$ octahedra in ME-POs based on the size of the A-cations, and it shows that the tilting of the octahedra follows a similar trend as *t*.

A strong increase in the tilting is observed accompanied by the increase of $\varepsilon$ from 0.198 in $La(5B_{0.2})O_3$ to 0.633 in $(5A_{0.2})(5B_{0.2})O_3$, followed by 1.609 in $Gd(5B_{0.2})O_3$. The lowering of symmetry due to the structural distortion is often found to be accompanied by a lowering of the coordination number of the A-site cations [17,21,22]. Hence, the effective coordination number (ECoN) for both the A- and B-site elements are calculated following the formulation proposed by Hoppe [23] and are listed in Table 2. The details of the ECoN calculation together with the refined distances of the A-O, as well as B-O are provided in the Supplementary Information (see Table S7 and related discussion). From the calculated ECoN values, it can be seen that for all ME-POs the B-site cations are almost ideally octahedrally coordinated independent of the type of cations present in the A- or B-sites. However, a large deviation from the ideal 12-fold coordination of the A-site cations is observed for all systems. The ECoN(A) also follows the similar trend as *t*, $\varepsilon$ and the degree of tilting of the $BO_6$ octahedra, i.e., a gradual decrease (from the ideal 12-fold coordination) on addition or substitution of the smaller cation at A-site or larger cation on the B-site. The origin of secondary phases observed in some of the systems can be strongly related to structural distortions in the lattices. In case of the $(5A_{0.2})MnO_3$ system, the strong Jahn-Teller distortion can be one of the plausible reasons for the high metric distortion (2.299) and the low ECoN(A) (6.12) and ECoN(B) (5.48) value. From the $\varepsilon$ vs. *t*, ECoN(A) vs. *t*

and ECoN(B) vs. *t* plots (Figure 4 (a),(b) and (c), respectively) it can be observed that the system which deviates most from the otherwise fairly linear behaviour is the $(5A_{0.2})MnO_3$ system. This indicates a strong enthalpic contribution due the possible Jahn-Teller distortion, which in turn can be prohibitive for the formation of a single phase perovskite structure in $(5A_{0.2})MnO_3$ at lower temperature (see Sec. 3.4 for the high temperature studies of this system). In $Y(5B_{0.2})O_3$, one possible reason for the formation of multiple phases can be the small size of $Y^{3+}$ and its inclination towards a lower coordination state. For the other systems the following reasons can be possible for the formation of the multiphase mixtures: (i) The chemical nature of the B-site with most stable oxidation states other than 3+ is found to prohibit the formation of a single phase in the case of a multicomponent equiatomic A-site configuration, for example in case of $(5A_{0.2})NiO_3$ the difficulty to stabilise $Ni^{3+}$ (under the synthesis conditions used) could plausibly explain the formation of high amount bunsenite (NiO) phase along with of major monoclinic type non-perovskite phase. (ii) Even for compositions which allow for the formation of perovskite type phase only, segregation of larger from smaller A-site cations along with the Jahn-Teller effect can be prohibitive for the formation of a single phase, as seen in $(5A_{0.2})MnO_3$. Therefore, these above mentioned factors can decrease the absolute of enthalpy of formation of a single phase compound and hence, favour the formation of non-single phase (either with non-perovskite type impurities or multi perovskite-type phase) compositions. Thus, considering all these factors and the fact that several of the heptanary ME-POs are not phase pure makes the chemically complex single phase 10-cationic system interesting.

**3.3. Chemical homogeneity.** A detailed TEM study was carried out on the 10-cationic system. On all regions of the sample investigated by TEM, perfect crystallinity has been observed, evident from the sharp lattice fringes shown in the HRTEM micrographs (Figure 5a and c). The fast Fourier transformations (FFTs) of the HRTEM micrographs are shown in Figure 5b and 5d, respectively. The FTTs can be indexed to a single orthorhombic perovskite (*Pbnm*) structure, which is in agreement with XRD findings. To substantiate the local homogeneity of the element distribution in the 10-cationic system, STEM-EELS/EDX spectra imaging was conducted (Supplementary Information Figure S13). Due to the heavily overlapped signals in the EDX spectra caused by the presence of multiple cations (i.e., ten), the elemental distribution maps

were mostly extracted from the EELS using the $M_{4,5}$ edges for Gd, Nd and Sm, only $M_5$ edge for La (since La $M_4$ overlaps with Ni $L_3$) and the $L_{2,3}$ edges for Co, Cr, Fe and Mn. The Y and Ni maps were constructed from EDX Y L and Ni K signals, respectively. These maps represent the distribution of the elements qualitatively and show that all the elements are uniformly distributed without any significant fluctuations down to nanometer scale. This confirms the local homogeneity in the studied 10 cationic system. Figure 6 shows a HAADF-STEM image for $(5A_{0.2})(5B_{0.2})O_3$ system along the [010] zone axis. The atomic layers of A-site containing heavy rare earth cations can be easily distinguished from the light transition metal cations on the B-site by the Z-contrast (here Z is average atomic number for site A and B, respectively). The atomic columns at the A-site show similar contrast indicating a random occupancy of the rare earth cations (Gd, La, Nd, Sm and Y). Similar conclusion can be drawn for the B-site cations confirming the random distribution of Co, Cr, Fe, Mn and Ni, as well.

**3.4. Possible reasons for the stabilisation of single phase.** In section 3.2 it has been mentioned that factors like ion-size mediated segregation and affinity of an element towards particular oxidation state (and co-ordination number) can increase the enthalpy of mixing ($\Delta H_{mix}$) for formation of the single phase. Hence, these factors stabilise the multiphase mixtures. Thus considering these facts, the high configurational entropy in these ME-PO systems can be one of the plausible reasons for the formation of the single phase, especially in case of the 10-cationic system. In case of multi-principal elemental alloys, better known as the high entropy alloys (HEAs), the high configurational entropy is often regarded as the reason for the formation of single phase structures in chemically complex systems. Similar entropic behaviour in stabilisation of a single phase was also observed in rocksalt based high entropy oxides (HEOs) by Rost *et al*. [1]. In case of the ME-POs the configurational entropy ($\Delta S_{config}$) can be calculated using the following formula:

$$\Delta S_{config} = -R[(\sum_{a=1}^{n} x_a \, lnx_a)_{A-site} + (\sum_{b=1}^{n} x_b \, lnx_b)_{B-site} + 3(\sum_{c=1}^{n} x_c \, lnx_c)_{O-site}] \qquad (7)$$

where $x_a$, $x_b$ and $x_c$ are the mole fraction of the ions present in the A-site, B-site and O-site (or the anion site which is oxygen in this case), respectively. For the $\Delta S_{config}$ calculations, all the ME-POs are considered to be stoichiometric, i.e., the possible oxygen defects that can be present are

not taken into account. For 10-cationic system, $(5A_{0.2})(5B_{0.2})O_3$, $S_{config}$ is 3.22R (0.0268 kJ $mol^{-1}$ $K^{-1}$) and is twice that of the other systems, 1.61R (0.0134 $kJ \cdot mol^{-1} \cdot K^{-1}$) in which only one of the sites, either A- or B-sites, are substituted by 5 equiatomic cations, $(5A_{0.2})BO_3$ or $A(5B_{0.2})O_3$. The competing factors of enthalpy and entropy are generally described within the approximation of an ideal solid solution. Independent of the systems (whether it is an alloy or an oxide), whenever a non-identical species is added to an existing sub-lattice, two thermodynamically opposing factor come into existence; one is the change of $\Delta H_{mix}$ which hinders the stability of the solid solution and the other is the entropic ($\Delta S_{mix}$ /$\Delta S_{config}$) gain from the mixing which supports the formation of the solid solution. The existence of the high $\Delta S_{mix}$ (or $\Delta S_{config}$) (calculated from Equation 7) due to the presence of several elements in the ME-PO systems cannot be ignored, independent of whether it actually plays a role in the structural stabilisation or not. In case of rocksalt based HEOs [1], a reversible transformation from multiphase to single phase structure was observed upon cyclic heat treatment. At higher temperature the $T\Delta S$ term becomes dominant over the $\Delta H$ term, hence decreasing the free energy (as $\Delta G_{mix} = \Delta H_{mix} - T\Delta S_{mix}$).

Thus, in order to investigate the role of entropy in the structural stabilisation, in-situ high temperature XRD (HTXRD) measurements were performed on the ME-POs. For the $(5A_{0.2})MnO_3$ system, where a series of perovskite phases (see Figure 3) are observed, in-situ HTXRD was performed at various temperatures (Figure 7a). A gradual transformation from a multiphase to a single phase accompanied by distinct changes in the XRD pattern is observed with increasing temperature (Figure 7a and b). A table with the details of the lattice parameters and phase composition of the powder at each temperature has been provided in the Supplementary Information (see Table S8).

The complete transformation to single perovskite type phase in $(5A_{0.2})MnO_3$ is found to occur around 900 °C. The Rietveld refinement for the same has been shown in the Figure 8. The single phase, thus obtained is preserved even at higher temperature 1000 °C, however, a complete reversion, i.e., a series of perovskite phases is observed while cooling back to room temperature (Figure 7). This behaviour is very similar to the one observed in case of the rocksalt based HEOs [1], where entropic factors were found to be the reason for the stabilisation of single phase compounds at elevated temperature. Hence, a similar entropic stabilisation is likely to be true in

case of the $(5A_{0.2})MnO_3$ system as well, since at higher temperature the $T\Delta S_{mix}$ term compensates the high $\Delta H_{mix}$ which is indicated to be especially high for the $(5A_{0.2})MnO_3$ system owing to the possible Jahn-Teller effect (see previous section 3.2). HTXRD patterns of the 10-cationic system show that the single phase is preserved all along (till 1000 °C) and no phase transformation is observed at lower temperature (Supplementary Information Figure S12). This is explained as follows: (i) the entropy of mixing can be large enough compared to the enthalpy of mixing, i.e., $\Delta S_{mix} >> \Delta H_{mix}$, making $\Delta G_{mix}$ independent of $\Delta H_{mix}$, even at lower temperatures, or (ii) even though the enthalpic penalty is larger than $T\Delta S_{mix}$ at lower temperature, the kinetics plays a limiting role (owing to the sluggish diffusion due to presence of several different cations). However, considering the facts that high configurational entropy is inherently present in these systems, one of the heptanary systems show reversible phase transformation as observed in rocksalt based HEOs [1,4], and the 10-cationic system is phase pure (in spite of its high chemical complexity) points towards the dominant role of entropy in structural stabilisation in the ME-POs. HTXRD measurements were done on all the other systems as well (see Supplementary Information Figure S15 (a-d) & Figure S16 (a-d)). In case of the multiple phase systems ($(5A_{0.2})CrO_3$, $(5A_{0.2})NiO_3$, $Sm(5B_{0.2})O_3$ and $Y(5B_{0.2})O_3$) single phase could not be achieved even at higher temperatures. This further proves the fact that in these systems the enthalpic penalties needed to stabilise the single phase is very high. Hence, supports the fact that the 10-cationic system is most likely entropy stabilised.

It is also interesting that in spite of the presence of so many elements in ME-POs (especially for the 10-cationic system) the orthorhombic distortion of the perovskite phase can be maintained, even at high temperatures (see Supplementary Information Figure S12 and Table S9), instead of formation of a highly symmetric cubic aristotype structure, which is known to be formed for many multinary systems. The tendency to maintain a high symmetry is also observed in the rocksalt type entropy stabilised oxide [1] and the fluorite type multicomponent rare earth oxides [7], where distortion and ordering variants are well known for both systems [24]. Hence, the tilting of the octahedra can be assumed to have an enthalpic contribution (similar to the Jahn-Teller contribution in Cu enriched HEOs) [25] in stabilisation of the lower symmetry perovskite phase. This distortion is known to result from the lowering of the A-site coordination, and

apparently this enthalpic contribution is so strong that the adoption of the cubic aristotype is energetically costly. This is further confirmed by a HT-study of the ME-POs system with the lowest deviation from the cubic symmetry (i.e. lowest value of strain $\varepsilon$, see Table 2), $La(5B_{0.2})O_3$. This phase can also not be transformed to a cubic structure, even at higher temperatures. However, in case of the $La(5B_{0.2})O_3$, a reversible structural transition from an orthorhombic (*Pbnm*) phase to a trigonal ($R\bar{3}ch$) phase is observed (Figure 9). The transformation starts around 125 °C but a distinctive change in the in-situ XRD patterns of $La(5B_{0.2})O_3$ can only be observed above 140 °C. Complete transformation to a trigonal structure takes place around 300 °C, where the volume of both the phase fractions, i.e., the trigonal cell and the orthorhombic cell become equal (see Supplementary Information Figure S17 and S18 and Table S10). The trigonal structure formed is preserved even at higher temperatures 1050 °C. This explains the fact that the octahedral tilting even in this systems (where the $t$ = 0.963 and $\varepsilon$ = 0.198) plays a crucial role in prohibiting the system to attain a cubic structure.

## CONCLUSIONS

Based on the results obtained from the combine XRD, ICP-MS, TEM and STEM/EDX-EELS studies, three major conclusions can be drawn:

i. Out of the eleven different ME-PO systems synthesised, six of the systems can be stabilised as a single phase perovskite type compound at ambient temperature. Even the 10-cationic $((Gd_{0.2}La_{0.2}Nd_{0.2}Sm_{0.2}Y_{0.2})(Co_{0.2}Cr_{0.2}Fe_{0.2}Mn_{0.2}Ni_{0.2})O_3)$ system is phase pure along with random and homogenous cation distribution on the respective sites, in spite of its high chemical complexity for which strong stabilisation of distinct binary combinations could be expected.

ii. The fact that five of the heptanary systems are multiphase mixtures whereas the 10-cationic system is phase pure indicates the possible role of unfavourable enthalpic interactions of some of the lower entropy (heptanary) systems which cannot be overcome by the entropic contribution. This indicates a possible role of entropy in the structural stabilisation.

iii. The signature of entropy driven structural stabilisation effect in these perovskites systems is strongly supported by the fact that the $(Gd_{0.2}La_{0.2}Nd_{0.2}Sm_{0.2}Y_{0.2})MnO_3$ system shows a

reversible transformation from a multiphase to single phase upon cyclic heat treatment. At higher temperature the single phase solid solution is favoured over the multiphase mixtures as the entropic ($T\Delta S_{mix}$) term dominates the free energy landscape. This is a typical entropy stabilisation behaviour, which has been reported only for the rocksalt based multicomponent equiatomic oxides. Hence, this study extends the concept of entropy driven structural stabilisation to multicomponent perovskite type oxides.

iv. Large metric distortion from the cubic symmetry along with strong tilting of the $BO_6$ polyhedra and lowering of the effective coordination number of A-site cation is observed for the systems with smaller cations on the A-site and/or larger B-site cations. The enthalpic factors like cation-size-adopted metric distortion, affinity of certain elements towards a particular oxidation state and Jahn-Teller distortion which favour an ordered scenario can possibly make the formation of a cubic aristotype structure in ME-POs, energetically expensive.

Future studies will focus on the deeper understanding of the local structure of these systems along with the functional properties for their complete exploitation.

## CONFLICTS OF INTEREST

There are no conflicts of interest to declare.

## ACKNOWLEDGMENT

The authors would like to thank the Helmholtz Association (Germany) for financial support through the Helmholtz Portfolio Project "Electrochemical Storage in Systems - Reliability and Integration". O.C. gratefully acknowledges support within an Emmy Noether Fellowship from the German Research Foundation (CL551/2-1). A.S. thanks Dr. Leonardo Velasco and Sree Harsha Nandam (Karlsruhe Institute of Technology, Germany) for fruitful discussions.

**REFERENCES**

[1] C.M. Rost, E. Sachet, T. Borman, A. Moballegh, E.C. Dickey, D. Hou, J.L. Jones, S. Curtarolo, J.-P. Maria, Entropy-stabilised oxides, Nat. Commun. 6 (2015) 8485. doi:10.1038/ncomms9485.

[2] B.S. Murty, J.W. Yeh, S. Ranganathan, High-Entropy Alloys, Butterworth- Heinemann, London, 2014. doi:10.1016/B978-0-12-800251-3.00010-9.

[3] J.W. Yeh, S.K. Chen, S.J. Lin, J.Y. Gan, T.S. Chin, T.T. Shun, C.H. Tsau, S.Y. Chang, Nanostructured high-entropy alloys with multiple principal elements: Novel alloy design concepts and outcomes, Adv. Eng. Mater. 6 (2004) 299–303+274. doi:10.1002/adem.200300567.

[4] A. Sarkar, R. Djenadic, N.J. Usharani, K.P. Sanghvi, V.S.K. Chakravadhanula, A.S. Gandhi, H. Hahn, S.S. Bhattacharya, Nanocrystalline multicomponent entropy stabilised transition metal oxides, J. Eur. Ceram. Soc. 37 (2017) 747–754. doi:10.1016/j.jeurceramsoc.2016.09.018.

[5] D. Bérardan, S. Franger, D. Dragoe, A.K. Meena, N. Dragoe, Colossal dielectric constant in high entropy oxides, Phys. Status Solidi - Rapid Res. Lett. 10 (2016) 328–333. doi:10.1002/pssr.201600043.

[6] D. Bérardan, S. Franger, A.K. Meena, N. Dragoe, Room temperature lithium superionic conductivity in high entropy oxides, J. Mater. Chem. A. 4 (2016) 9536–9541. doi:10.1039/C6TA03249D.

[7] R. Djenadic, A. Sarkar, O. Clemens, C. Loho, M. Botros, V.S.K. Chakravadhanula, C. Kübel, S.S. Bhattacharya, A.S. Gandhi, H. Hahn, Multicomponent equiatomic rare earth oxides, Mater. Res. Lett. 5 (2017) 102–109. doi:10.1080/21663831.2016.1220433.

[8] A. Sarkar, C. Loho, L. Velasco, T. Thomas, S.S. Bhattacharya, H. Hahn, R. Djenadic, Multicomponent equiatomic rare earth oxides with a narrow band gap and associated praseodymium multivalency, Dalt. Trans. 46 (2017) 12167–12176.

doi:10.1039/C7DT02077E.

[9] S. Jiang, T. Hu, J. Gild, N. Zhou, J. Nie, M. Qin, T. Harrington, K. Vecchio, J. Luo, A new class of high-entropy perovskite oxides, Scr. Mater. 142 (2018) 116–120. doi:10.1016/j.scriptamat.2017.08.040.

[10] C.J. Howard, B.J. Campbell, H.T. Stokes, M.A. Carpenter, R.I. Thomson, Crystal and magnetic structures of hexagonal YMnO 3, Acta Crystallogr. Sect. B Struct. Sci. Cryst. Eng. Mater. 69 (2013) 534–540. doi:10.1107/S205251921302993X.

[11] G.L. Messing, S.-C. Zhang, G. V. Jayanthi, Ceramic Powder Synthesis by Spray Pyrolysis, J. Am. Ceram. Soc. 76 (1993) 2707–2726. doi:10.1111/j.1151-2916.1993.tb04007.x.

[12] R. Djenadic, M. Botros, C. Benel, O. Clemens, S. Indris, A. Choudhary, T. Bergfeldt, H. Hahn, Nebulized spray pyrolysis of Al-doped Li7La3Zr2O12 solid electrolyte for battery applications, Solid State Ionics. 263 (2014) 49–56. doi:10.1016/j.ssi.2014.05.007.

[13] C.A. Schneider, W.S. Rasband, K.W. Eliceiri, NIH Image to ImageJ: 25 years of image analysis, Nat. Methods. 9 (2012) 671–675. doi:10.1038/nmeth.2089.

[14] Topas V5, General profile and structure analysis software for powder diffraction data, User's Manual, Bruker AXS, Karlsruhe, Germany, 2015.

[15] R.D. Shannon, Revised effective ionic radii and systematic studies of interatomic distances in halides and chalcogenides, Acta Crystallogr. Sect. A. 32 (1976) 751–767. doi:10.1107/S0567739476001551.

[16] V.M. Goldschmidt, Die Gesetze der Krystallochemie, Naturwissenschaften. 14 (1926) 477–485. doi:10.1007/BF01507527.

[17] O. Clemens, M. Gröting, R. Witte, J.M. Perez-Mato, C. Loho, F.J. Berry, R. Kruk, K.S. Knight, A.J. Wright, H. Hahn, P.R. Slater, Crystallographic and Magnetic Structure of the Perovskite-Type Compound BaFeO 2.5 : Unrivaled Complexity in Oxygen Vacancy Ordering, Inorg. Chem. 53 (2014) 5911–5921. doi:10.1021/ic402988y.

[18] R.J.D. Tilley, Perovskites: Structure-Property Relationships, John Wiley & Sons, Ltd, West Sussex, 2016.

[19] A.D. Aljaberi, J.T.S. Irvine, Crystal structure of A-site deficient La 0.2 Sr 0.7−x Ca x TiO 3 perovskite at ambient conditions and high temperatures: a neutron powder diffraction study, Dalt. Trans. 44 (2015) 10828–10833. doi:10.1039/C5DT00238A.

[20] J.A. Alonso, M.J. Martínez-Lope, M.T. Casais, M.T. Fernández-Díaz, Evolution of the Jahn−Teller Distortion of MnO 6 Octahedra in RMnO 3 Perovskites (R = Pr, Nd, Dy, Tb, Ho, Er, Y): A Neutron Diffraction Study, Inorg. Chem. 39 (2000) 917–923. doi:10.1021/ic990921e.

[21] O. Clemens, M. Kuhn, R. Haberkorn, Synthesis and characterization of the La1−xSrxFeO3−δ system and the fluorinated phases La1−xSrxFeO3−xFx, J. Solid State Chem. 184 (2011) 2870–2876. doi:10.1016/j.jssc.2011.08.037.

[22] O. Clemens, R. Haberkorn, P.R. Slater, H.P. Beck, Synthesis and characterisation of the SrxBa1−xFeO3−y-system and the fluorinated phases SrxBa1−xFeO2F, Solid State Sci. 12 (2010) 1455–1463. doi:10.1016/j.solidstatesciences.2010.06.002.

[23] R. Hoppe, Effective coordination numbers (ECoN) and mean fictive ionic radii (MEFIR), Zeitschrift Für Krist. 150 (1979) 23–52. doi:10.1524/zkri.1979.150.1-4.23.

[24] U. Mller, Inorganic Structural Chemistry, John Wiley & Sons, Ltd, Chichester, UK, 2006. doi:10.1002/9780470057278.

[25] D. Berardan, A.K. Meena, S. Franger, C. Herrero, N. Dragoe, Controlled Jahn-Teller distortion in (MgCoNiCuZn)O-based high entropy oxides, J. Alloys Compd. 704 (2017) 693–700. doi:10.1016/j.jallcom.2017.02.070.

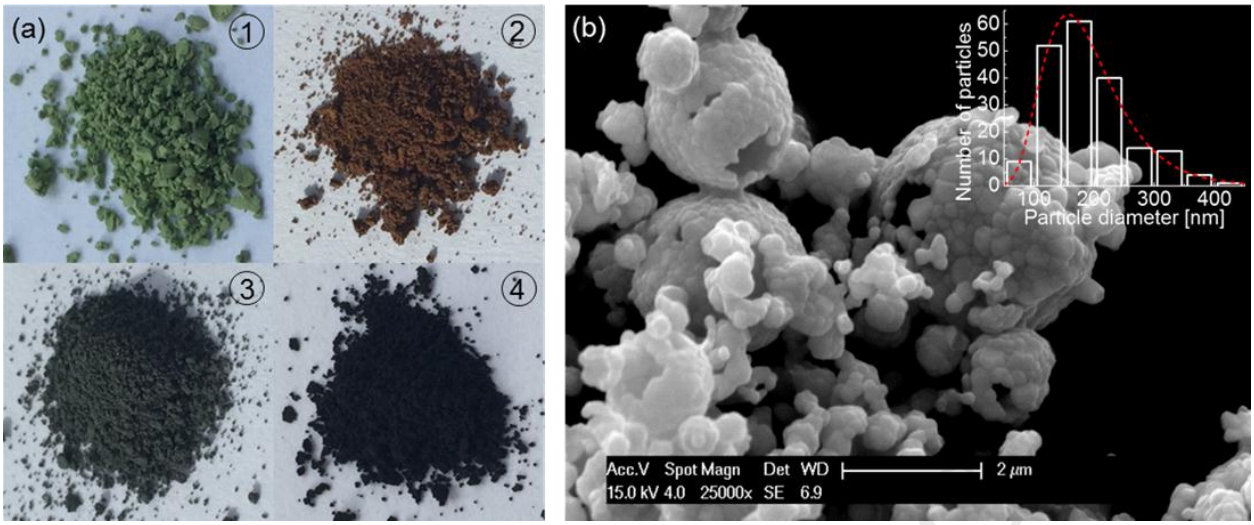


**Figure 1.** (a) Photographs of several ME-PO systems showing variation in powder colour: 1. $(5A_{0.2})CrO_3$, 2. $(5A_{0.2})FeO_3$, 3. $(5A_{0.2})NiO_3$, 4. $(5A_{0.2})(5B_{0.2})O_3$. (b) SEM micrograph of $(5A_{0.2})(5AB_{0.2})O_3$ powder representing a typical morphology of ME-POs systems produced by NSP method. Inset represents log-normal particle size distribution with an average particle size of 180 nm.

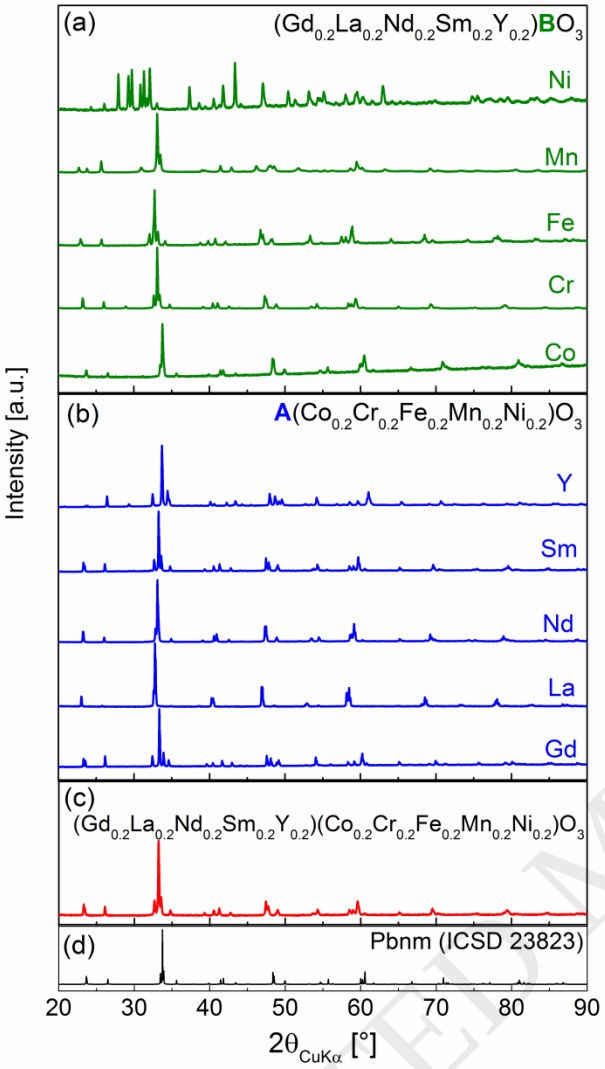


**Figure 2.** XRD patterns of ME-PO powders: (a) $(5A_{0.2})BO_3$, B = Co, Cr, Fe, Mn, or Ni, (b) $A(5B_{0.2})O_3$, A = Gd, La, Nd, Sm, or Y, (c) $(5A_{0.2})(5B_{0.2})O_3$, and (d) simulated orthorhombic perovskite (*Pbnm*) pattern (ICSD 23823).

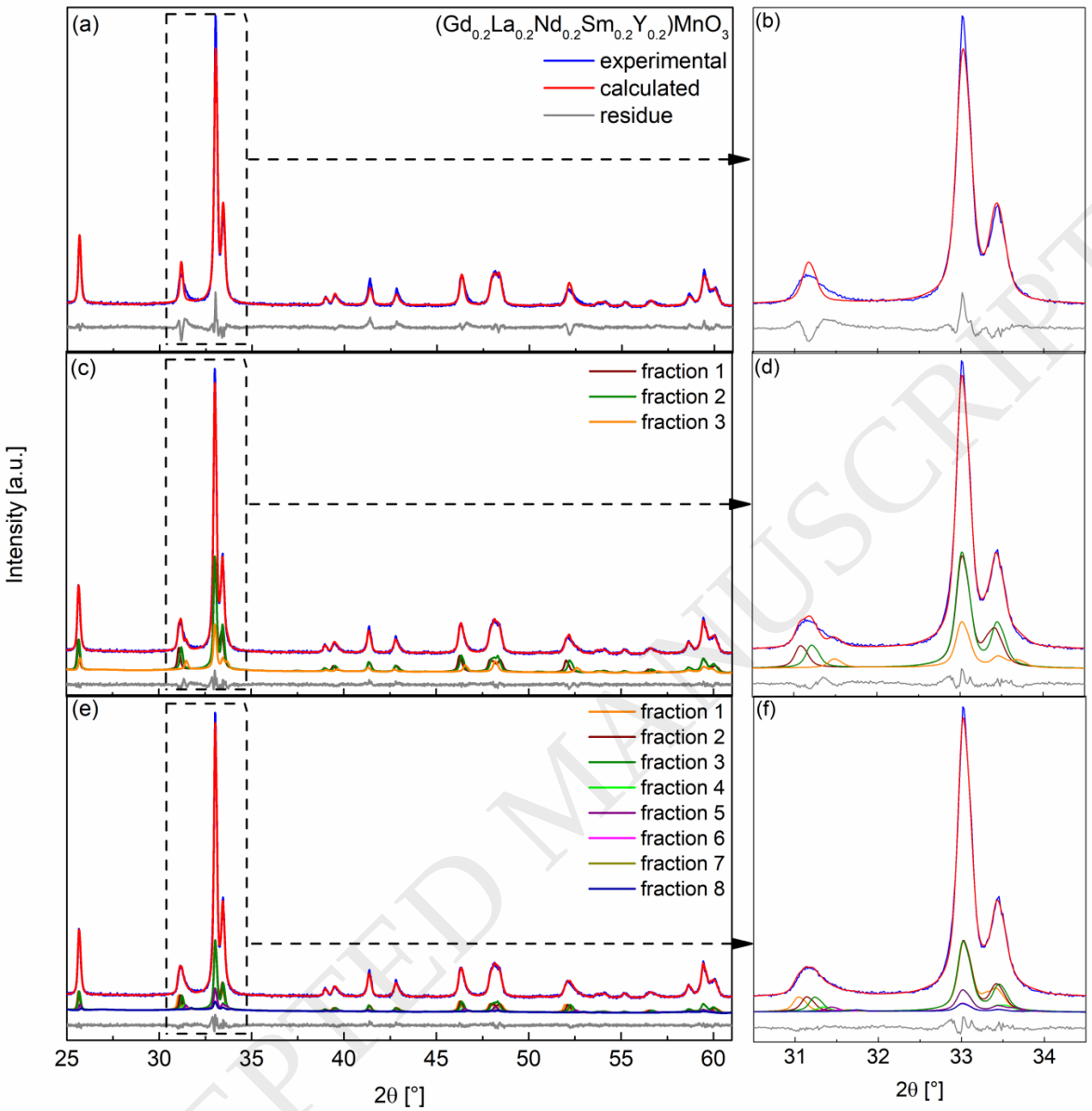


**Figure 3.** XRD pattern together with Rietveld fit of $(5A_{0.2})MnO_3$, where either a single (a), 3 (b) or 8 (c) perovskite phases are used to refine the structure. The zoomed in section (b, d and f) shows that a good fit can be achieved with a strongly constrained distribution model of perovskite phases.

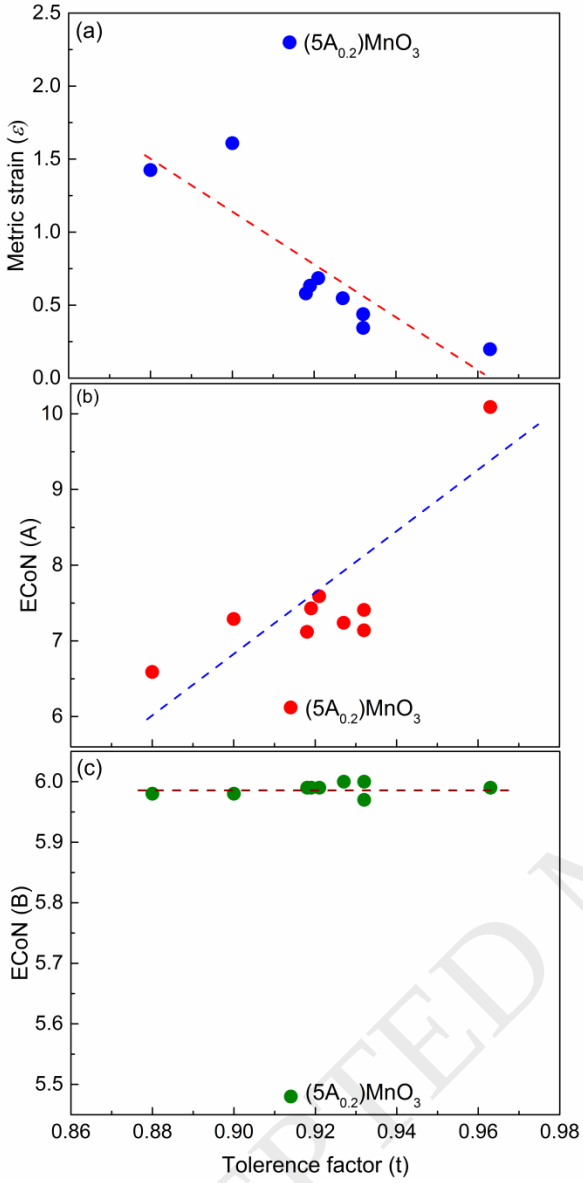


**Figure 4.** Metric distortion **(**$\varepsilon$), EcoN(A) and ECoN(B) are plotted with respect to the tolerance factor (*t*) in diagram (a), (b) and (c) respectively. A strong deviation of the $(5A_{0.2})MnO_3$ system from the otherwise fairly linear behaviour can be observed.

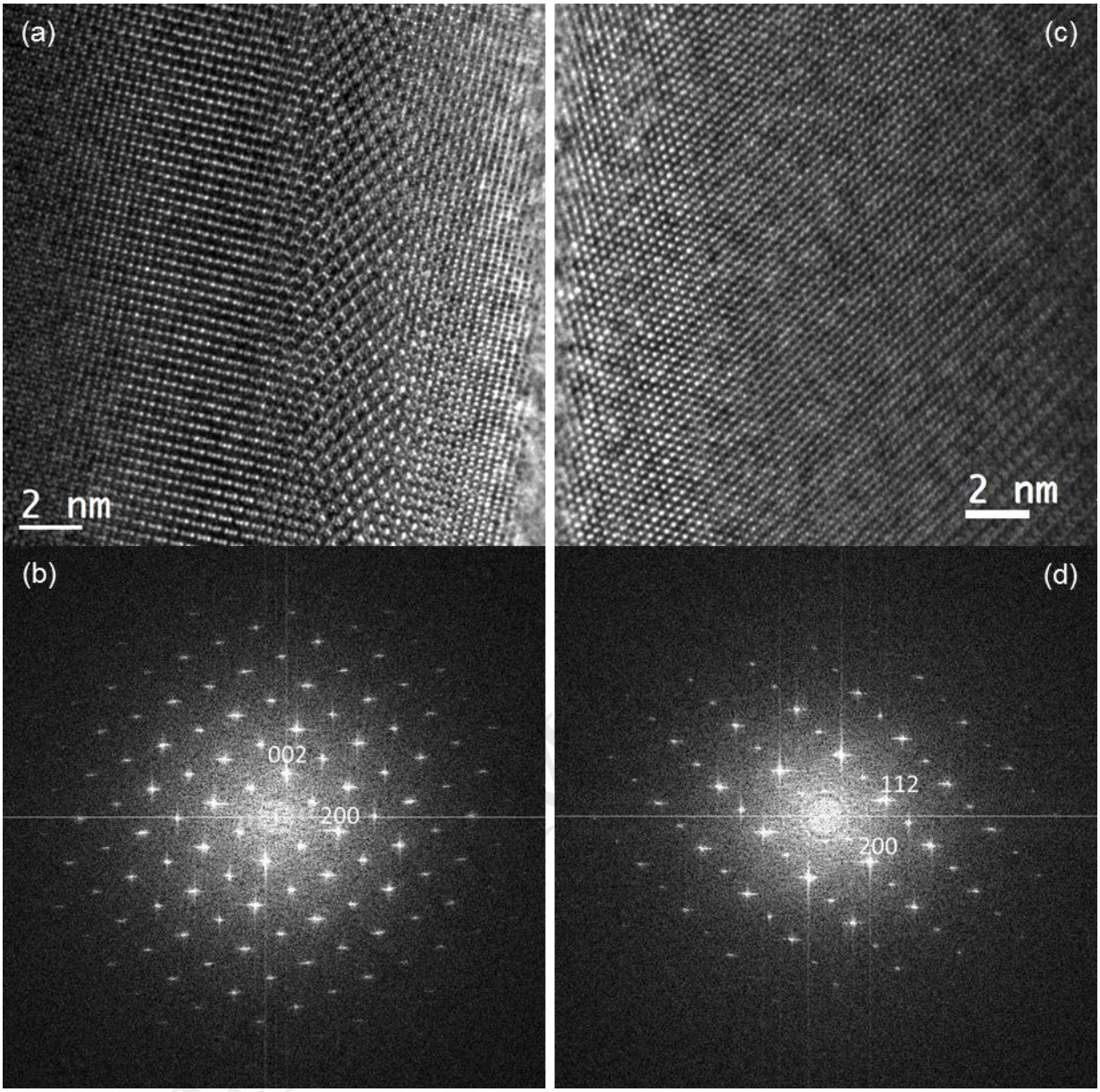


**Figure 5.** HR-TEM micrographs and corresponding FFTs, respectively for $(5A_{0.2})(5B_{0.2})O_3$ system along the [010] (a, b) and $[02\bar{1}]$ (c, d) zone axes.

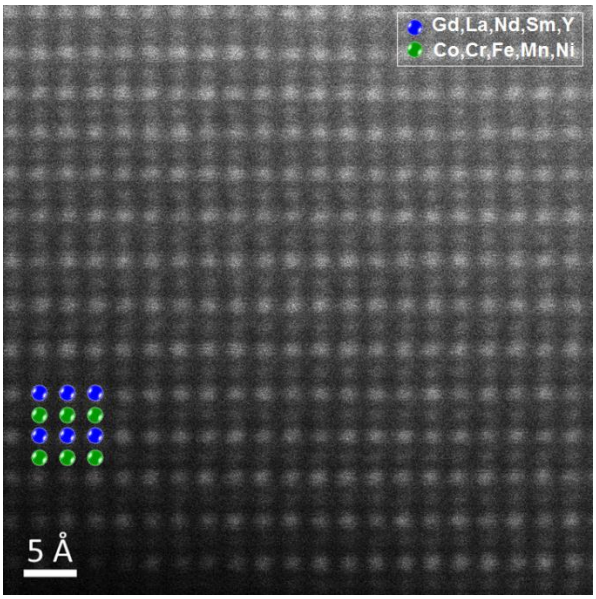


**Figure 6.** HAADF-STEM image taken along [010] zone axis, where the atomic layers containing heavier atoms (Gd, La, Nd, Sm and Y) and lighter atoms (Co, Cr, Fe, Mn and Ni), respectively can be clearly distinguished.

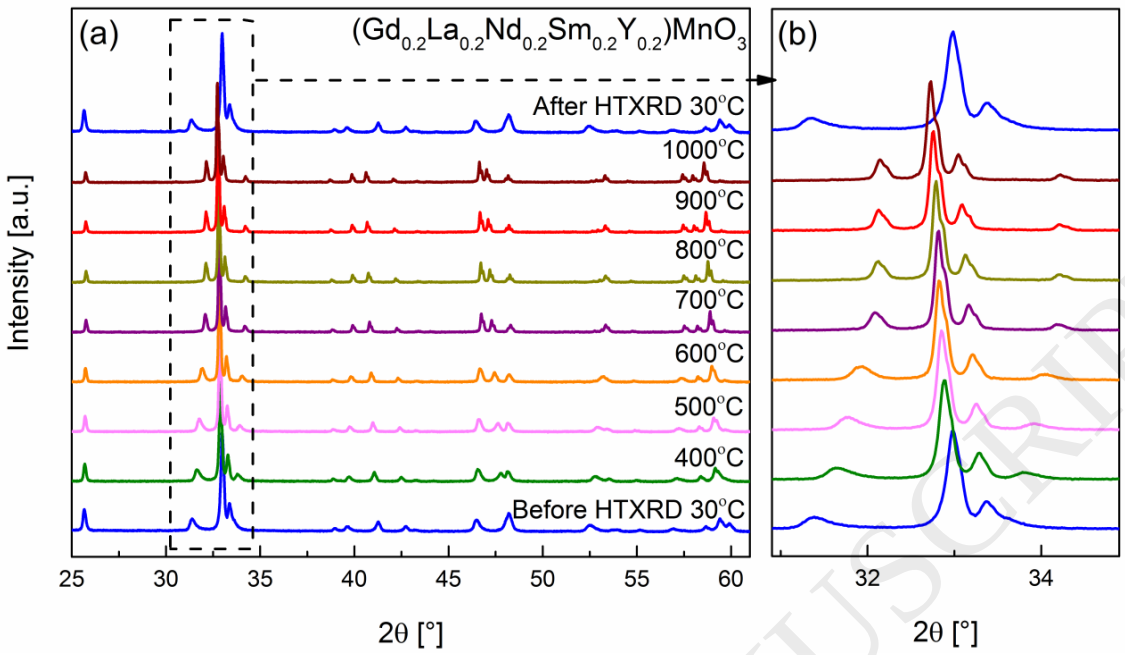


**Figure 7.** Full range (a) and magnified portion (b) of the in-situ HTXRD pattern of $(5A_{0.2})MnO_3$ at different temperatures. A reversible transformation from multiple phases to a single phase perovskite occurs around 900 °C.

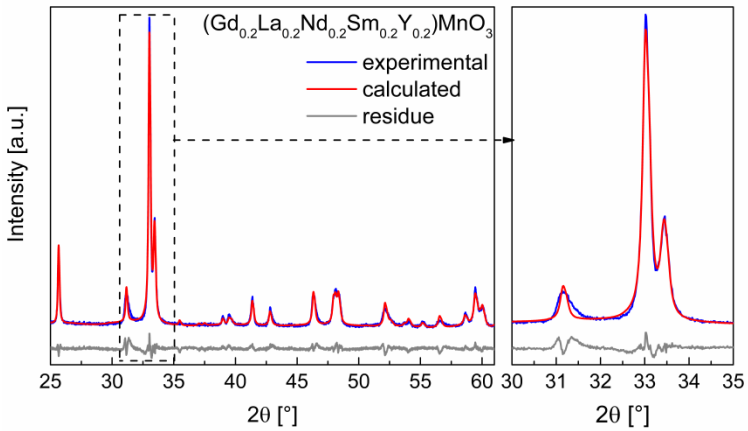


**Figure 8.** In-situ HTXRD pattern together with Rietveld fit of $(5A_{0.2})MnO_3$ at 900 °C. The pattern can be well fitted using only a single perovskite phase compared to the fit at room temperature where a minimum of three perovksite phases are needed to fit the pattern and to describe the peak shape due to demixing of A-site cations adequately.

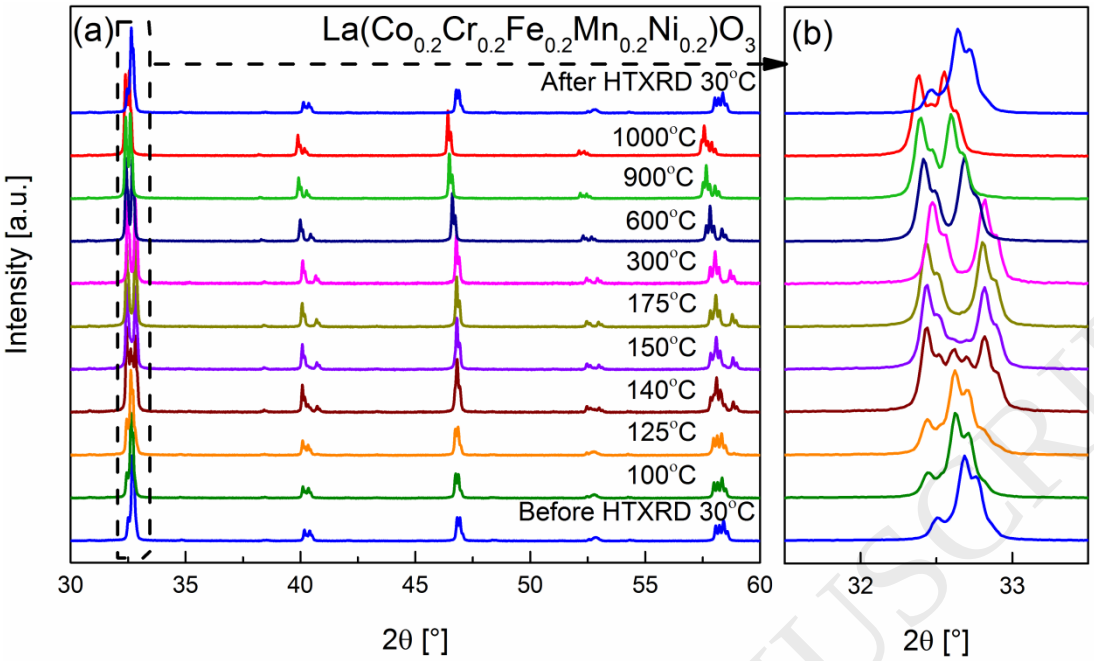


**Figure 9.** Full range (a) and magnified portion (b) of the in-situ HTXRD pattern of $La(5B_{0.2})O_3$ at different temperatures. Reversible structural transition from an orthorhombic to trigonal phase starts around 125 $^{o}$C and complete transition to a phase pure trigonal phase observed above 300 $^{o}$C.

**Table 1.** Structural data for all ME-POs systems obtained from Rietveld refinement: space group (SG) along with prototype structures of secondary phases, phase fraction ($f$ in wt.%), lattice parameters ($a$, $b$, $c$ in Å, and $\beta$ in °) and goodness of fit (GoF).

| ME-POs | SG | $f$ [wt.%] | $a$ [Å] | $b$ [Å] | $c$ [Å] | $\beta$ [°] | GoF |
|---|---|---|---|---|---|---|---|
| **$5A_{0.2}$ = $Gd_{0.2}La_{0.2}Nd_{0.2}Sm_{0.2}Y_{0.2}$** | | | | | | | |
| **$(5A_{0.2})CoO_3$** | *Pbnm* | 100 | 5.2964(2) | 5.3655(2) | 7.5128(3) | - | 1.16 |
| **$(5A_{0.2})CrO_3$** | *Pbnm*<br>$Ia\bar{3}$ ($Gd_2O_3$) | 97.7(6)<br>2.3(6) | 5.3799(7)<br>10.729(0) | 5.5035(7) | 7.6614(1) | - | 1.74 |
| **$(5A_{0.2})FeO_3$** | *Pbnm* | 100 | 5.4094(3) | 5.5936(2) | 7.7259(2) | - | 1.63 |
| **$(5A_{0.2})MnO_3$** | *Pbnm*<br>*Pbnm*<br>*Pbnm* | 42.3(1)<br>40.9(1)<br>16.8(5) | 5.3658(4)<br>5.3670(4)<br>5.3633(2) | 5.7396(4)<br>5.7637(5)<br>5.6916(2) | 7.5352(5)<br>7.5201(7)<br>7.5652(3) | -<br>-<br>- | 1.43 |
| **$(5A_{0.2})NiO_3$** | *C2/m* ($Sm_2O_3$)[#]<br>$Fm\bar{3}m$ (NiO)<br>*I4/mmm* ($La_2NiO_4$) | 60.4(3)<br>33.1(3)<br>6.5(1) | 14.259(4)<br>4.1791(1)<br>3.8465(3) | 3.6241(9)<br>-<br>- | 8.8706(2)<br>-<br>12.5330(2) | 100.6(0)<br>-<br>- | 1.27 |
| **$5B_{0.2}$ = $Co_{0.2}Cr_{0.2}Fe_{0.2}Mn_{0.2}Ni_{0.2}$** | | | | | | | |
| **$Gd(5B_{0.2})O_3$** | *Pbnm* | 100 | 5.2958(6) | 5.5303(6) | 7.5708(9) | - | 1.25 |
| **$La(5B_{0.2})O_3$** | *Pbnm* | 100 | 5.4656(6) | 5.5101(5) | 7.7424(9) | - | 1.19 |
| **$Nd(5B_{0.2})O_3$** | *Pbnm* | 100 | 5.4087(6) | 5.4760(6) | 7.6718(8) | - | 1.47 |
| **$Sm(5B_{0.2})O_3$** | *Pbnm*<br>*C2/m* ($Sm_2O_3$)[#] | 98.3(3)<br>1.7(3) | 5.3523(6)<br>14.236(1) | 5.5024(6)<br>3.6400(3) | 7.6178(9)<br>8.7290(1) | -<br>100.4(1) | 1.42 |
| **$Y(5B_{0.2})O_3$** | *Pbnm*<br>$Ia\bar{3}$ ($Y_2O_3$)<br>$Fm\bar{3}m$ (NiO) | 94.7(1)<br>3.2(7)<br>2.1(1) | 5.2255(6)<br>10.597(1)<br>4.2021(1) | 5.5361(7)<br>-<br>- | 7.4977(1)<br>-<br>- | -<br>-<br>- | 1.44 |
| **$(5A_{0.2})(5B_{0.2})O_3$** | *Pbnm* | 100 | 5.3614(7) | 5.5012(7) | 7.6309(1) | - | 1.45 |

[#]In $(5A_{0.2})NiO_3$ and $Sm(5B_{0.2})O_3$, the prototype structure used for the refinement of the *C2/m* phase is $Sm_2O_3$, however the composition of the phase is most likely to be $(5A_{0.2})_2O_3$.

**Table 2**. Overview of the Goldschmidt's factor (*t*), metric distortion (ε), and effective coordination number (ECoN) for A- and B-site elements in ME-PO systems obtained from ionic radii, lattice parameters of phase with perovskite structure and structural model, respectively.

| ME-POs | *t* | *ε* [%] | ECoN(A) | ECoN(B) |
|---|---|---|---|---|
| **$5A_{0.2}$ = $Gd_{0.2}La_{0.2}Nd_{0.2}Sm_{0.2}Y_{0.2}$** | | | | |
| **$(5A_{0.2})CoO_3$** | 0.932 | 0.344 | 7.41 | 6.00 |
| **$(5A_{0.2})CrO_3$** | 0.927 | 0.547 | 7.24 | 6.00 |
| **$(5A_{0.2})FeO_3$** | 0.918 | 0.580 | 7.12 | 5.99 |
| **$(5A_{0.2})MnO_3$** | 0.914 | 2.299 | 6.12 | 5.48 |
| **$(5A_{0.2})NiO_3$**[#] | 0.963 | - | - | - |
| **$5B_{0.2}$ = $Co_{0.2}Cr_{0.2}Fe_{0.2}Mn_{0.2}Ni_{0.2}$** | | | | |
| **$Gd(5B_{0.2})O_3$** | 0.900 | 1.609 | 7.29 | 5.98 |
| **$La(5B_{0.2})O_3$** | 0.963 | 0.198 | 10.09 | 5.99 |
| **$Sm(5B_{0.2})O_3$** | 0.921 | 0.685 | 7.59 | 5.99 |
| **$Nd(5B_{0.2})O_3$** | 0.932 | 0.438 | 7.14 | 5.97 |
| **$Y(5B_{0.2})O_3$** | 0.880 | 1.425 | 6.59 | 5.98 |
| **$(5A_{0.2})(5B_{0.2})O_3$** | 0.919 | 0.633 | 7.43 | 5.99 |

[#]Perovskite phase was not formed in this system.

# Supplementary Information

# Rare earth and transition metal based entropy stabilised perovskite type oxides

*Abhishek Sarkar,*[a,b] Ruzica Djenadic,[b,c,g] Di Wang,[a,d] Christina Hein,[e] Ralf Kautenburger,[e] Oliver Clemens,*[a,f] and Horst Hahn,*[a,b,c]*

[a]Institute of Nanotechnology, Karlsruhe Institute of Technology, Hermann-von-Helmholtz-Platz 1, 76344 Eggenstein-Leopoldshafen, Germany

[b]Joint Research Laboratory Nanomaterials – Technische Universität Darmstadt and Karlsruhe Institute of Technology, Alarich-Weiss-Str. 2, 64287 Darmstadt, Germany

[c]Helmholtz Institute Ulm – Electrochemical Energy Storage, Helmholtzstr. 11, 89081 Ulm, Germany

[d]Karlsruhe Nano Micro Facility, Karlsruhe Institute of Technology, Hermann-von-Helmholtz-Platz 1, 76344 Eggenstein-Leopoldshafen, Germany

[e]WASTe Group, Inorganic Chemistry, Saarland University, Campus Dudweiler, Am Markt Zeile 5, D-66125 Saarbrücken, Germany

[f]Materials Design by Synthesis Group, Technische Universität Darmstadt, Alarich-Weiss-Str. 2, 64287 Darmstadt, Germany

[g]Heraeus Deutschland GmbH & Co. KG, Heraeusstr. 12 – 14, 63450 Hanau, Germany

*Corresponding authors: abhishek.sarkar@kit.edu, oliver.clemens@nano.tu-darmstadt.de, horst.hahn@kit.edu

**Table S1.** Oxidation state, co-ordination number (CN) and corresponding cationic radii ($r_c$).[1]

| Element | Oxidation | CN | $r_c$ [Å] |
|---|---|---|---|
| **Gd** | 3+ | XII | 1.10 |
| **La** | 3+ | XII | 1.36 |
| **Nd** | 3+ | XII | 1.27 |
| **Sm** | 3+ | XII | 1.24 |
| **Y** | 3+ | XII | 1.07 |
| **Co** | 3+ | VI | $0.54^{LS}$, $0.61^{HS}$ |
| **Cr** | 3+ | VI | 0.61 |
| **Fe** | 3+ | VI | $0.54^{LS}$, $0.64^{HS}$ |
| **Mn** | 3+ | VI | $0.58^{LS}$, $0.64^{HS}$ |
| **Ni** | 3+ | VI | $0.56^{LS}$, $0.60^{HS}$ |

LS - low spin, HS - high spin

**Table S2.** Space groups of various perovskites oxides based on rare earth (A-site) and transition metal (B-site) elements showing that they can adopt different crystal structures.[2]

| System | Space group (number) |
|---|---|
| **$GdCoO_3$** | *Pbnm* (62) |
| **$GdCrO_3$** | *Pbnm* (62) |
| **$GdFeO_3$** | *Pbnm* (62) |
| **$GdMnO_3$** | *Pbnm* (62) |
| **$GdNiO_3$** | *Pbnm* (62) |
| **$LaCoO_3$** | $R\bar{3}ch$ (167) |
| **$LaCrO_3$** | *Pbnm (62)*<br>$Pm\bar{3}m$ *(221)* |
| **$LaFeO_3$** | *Pbnm* (62) |
| **$LaMnO_3$** | $R\bar{3}ch$ (167)<br>*Pnma* (62) |
| **$LaNiO_3$** | $R\bar{3}ch$ (167)<br>$Pm\bar{3}m$ (221) |
| **$NdCoO_3$** | *Pbnm* (62)<br>$Pm\bar{3}m$ (221) |
| **$NdCrO_3$** | *Pbnm* (62) |
| **$NdFeO_3$** | *Pbnm* (62) |
| **$NdMnO_3$** | *Pbnm* (62) |
| **$NdNiO_3$** | *Pbnm* (62) |
| **$SmCoO_3$** | $Pm\bar{3}m$ (221)<br>*Pbnm* (62) |
| **$SmCrO_3$** | $Pm\bar{3}m$ (221)<br>*Pbnm* (62) |
| **$SmFeO_3$** | *Pbnm* (62) |
| **$SmMnO_3$** | *Pbnm* (62) |
| **$SmNiO_3$** | *Pbnm* (62) |
| **$YCoO_3$** | *Pbnm* (62) |
| **$YCrO_3$** | *Pbnm* (62) |
| **$YFeO_3$** | *Pbnm* (62)<br>$P6_3/mmc$ (194) |
| **$YMnO_3$** | $P6_3cm$ (185) |
| **$YNiO_3$** | $P12_1/n1$ (14) |

**Table S3.** Operating parameters and analytical conditions of the ICP-MS

| ICP-MS | Agilent 7500cx |
|---|---|
| **RF Power** | 1550 W |
| **Cooling/auxiliary gas** | 15.0/1.05 L $min^{-1}$ |
| **Dwell times** | 300 ms (3 x 100 ms) per mass |
| **Helium gas flow for reaction mode** | 4.3 ml $min^{-1}$ |
| **Repetition** | 3 times |
| **Samples** | |
| **ICP standards** | Certipur® (Merck) |
| **Analysed isotopes (reaction mode)** | $^{52}Cr$, $^{56}Fe$ |
| **Analysed isotopes (default mode)** | $^{55}Mn$, $^{59}Co$, $^{60}Ni$, $^{89}Y$, $^{139}La$, $^{146}Nd$, $^{147}Sm$, $^{157}Gd$ |
| **Internal standards** | $^{45}Sc$, $^{165}Ho$ |

**Table S4.** Actual composition of the ME-POs based on ICP-MS analysis, showing that all cations in are present in desired stoichiometry. The compositions of all the elements are measured in triplicate and normalized in a way that the sum of the A-site stoichiometry is fixed to 1.

| System | Gd | La | Nd | Sm | Y | Co | Cr | Fe | Mn | Ni |
|---|---|---|---|---|---|---|---|---|---|---|
| $(5A_{0.2})CoO_3$ | 0.198(9) | 0.201(6) | 0.194(3) | 0.202(2) | 0.205(6) | 0.990(66) | - | - | - | - |
| $La(5B_{0.2})O_3$ | - | 1.000(22) | - | - | - | 0.212(8) | 0.207(11) | 0.202(8) | 0.216(10) | 0.206(6) |
| $Nd(5B_{0.2})O_3$ | - | - | 1.000(14) | - | - | 0.216(10) | 0.203(12) | 0.202(1) | 0.208(13) | 0.210(9) |
| $Sm(5B_{0.2})O_3$ | - | - | - | 1.000(63) | - | 0.200(13) | 0.186(9) | 0.188(8) | 0.201(12) | 0.201(1) |
| $(5A_{0.2})(5B_{0.2})O_3$ | 0.198(2) | 0.200(3) | 0.196(8) | 0.202(2) | 0.204(3) | 0.210(3) | 0.194(8) | 0.197(7) | 0.209(8) | 0.208(2) |

**Table S5.** Elemental composition based on EDS analysis of SEM micrographs showing that all cations in all three the systems are present in equiatomic amounts.

| System | Gd | La | Nd | Sm | Y | Co | Cr | Fe | Mn | Ni |
|---|---|---|---|---|---|---|---|---|---|---|
| **$(5A_{0.2})CoO_3$** | 10.1 | 10.8 | 10.0 | 10.2 | 11.0 | 47.8 | - | - | - | - |
| **$(5A_{0.2})CrO_3$** | 10.4 | 11.0 | 10.7 | 10.6 | 9.1 | - | 48.2 | - | - | - |
| **$(5A_{0.2})FeO_3$** | 10.8 | 10.9 | 10.3 | 10.6 | 9.3 | - | - | 48.1 | - | - |
| **$(5A_{0.2})MnO_3$** | 10.0 | 10.0 | 10.9 | 9.9 | 9.7 | - | - | - | 49.5 | - |
| **$(5A_{0.2})NiO_3$** | 9.9 | 9.8 | 9.2 | 9.8 | 10.2 | - | - | - | - | 51.1 |
| **$Gd(5B_{0.2})O_3$** | 48.8 | - | - | - | - | 10.2 | 10.6 | 10.2 | 10.5 | 9.7 |
| **$La(5B_{0.2})O_3$** | - | 49.0 | - | - | - | 10.2 | 10.6 | 10.3 | 9.5 | 10.3 |
| **$Nd(5B_{0.2})O_3$** | - | - | 48.9 | - | - | 10.3 | 10.6 | 9.1 | 11.2 | 9.9 |
| **$Sm(5B_{0.2})O_3$** | - | - | - | 50.1 | - | 9.5 | 9.9 | 10.5 | 10.9 | 9.1 |
| **$Y(5B_{0.2})O_3$** | - | - | - | - | 50.5 | 10.0 | 10.0 | 9.9 | 9.9 | 9.7 |
| **$(5A_{0.2})(5B_{0.2})O_3$** | 9.0 | 10.3 | 9.7 | 9.9 | 10.7 | 10.5 | 10.2 | 9.5 | 10.1 | 10.1 |

$5A_{0.2} = Gd_{0.2}La_{0.2}Nd_{0.2}Sm_{0.2}Y_{0.2}$, $5B_{0.2} = Co_{0.2}Cr_{0.2}Fe_{0.2}Mn_{0.2}Ni_{0.2}$

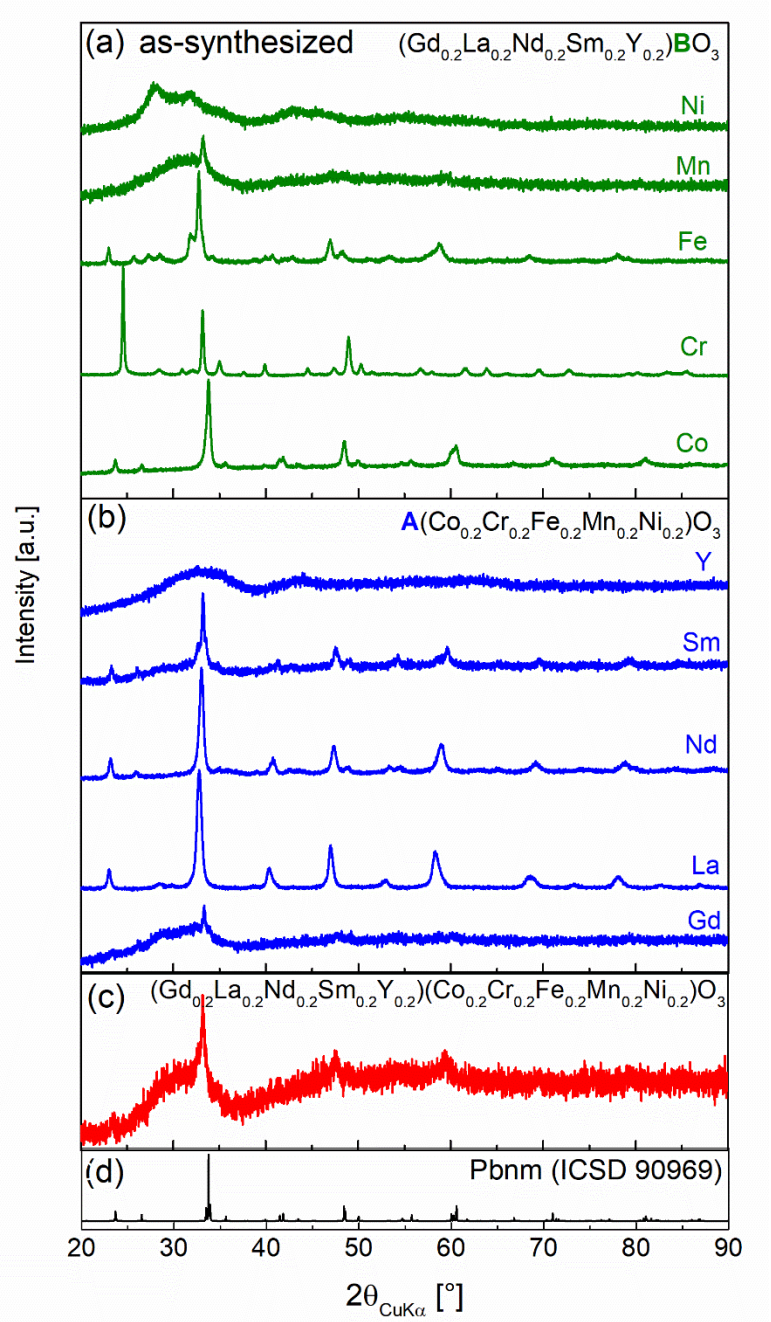


**Figure S1.** XRD patterns of as-synthesised ME-PO powders: (a) (5A0.2)BO3, B = Co, Cr, Fe, Mn, or Ni, (b) A(5B0.2)O3, A = Gd, La, Nd, Sm, or Y, (c) (5A0.2)(5B0.2)O3, and (d) simulated orthorhombic perovskite (Pbnm) pattern (ICSD 23823).

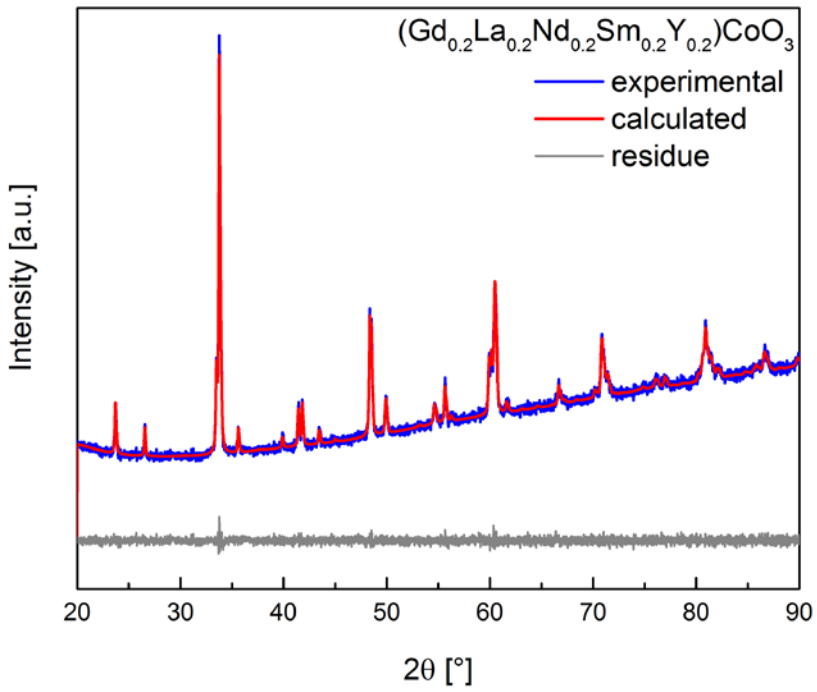


**Figure S2.** XRD pattern together with Rietveld fit of $(5A_{0.2})CoO_3$, confirming the phase purity (of the perovskite structure) of the powder.

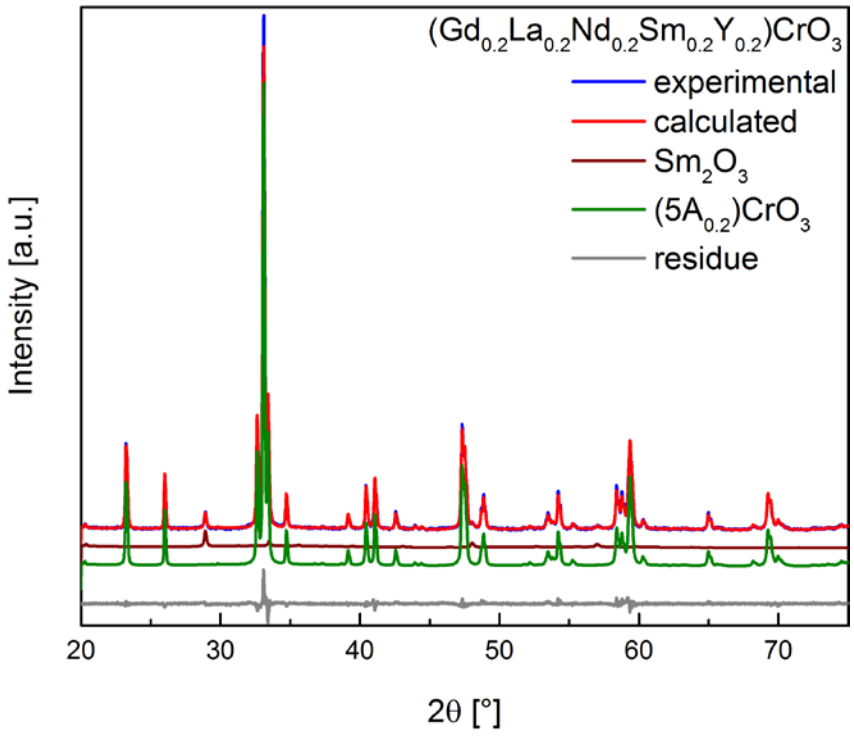


**Figure S3.** XRD pattern together with Rietveld fit of $(5A_{0.2})CrO_3$, confirming the presence of small amount (~ 3 wt.%) of secondary $Sm_2O_3$-type phase along with the major perovskite phase.

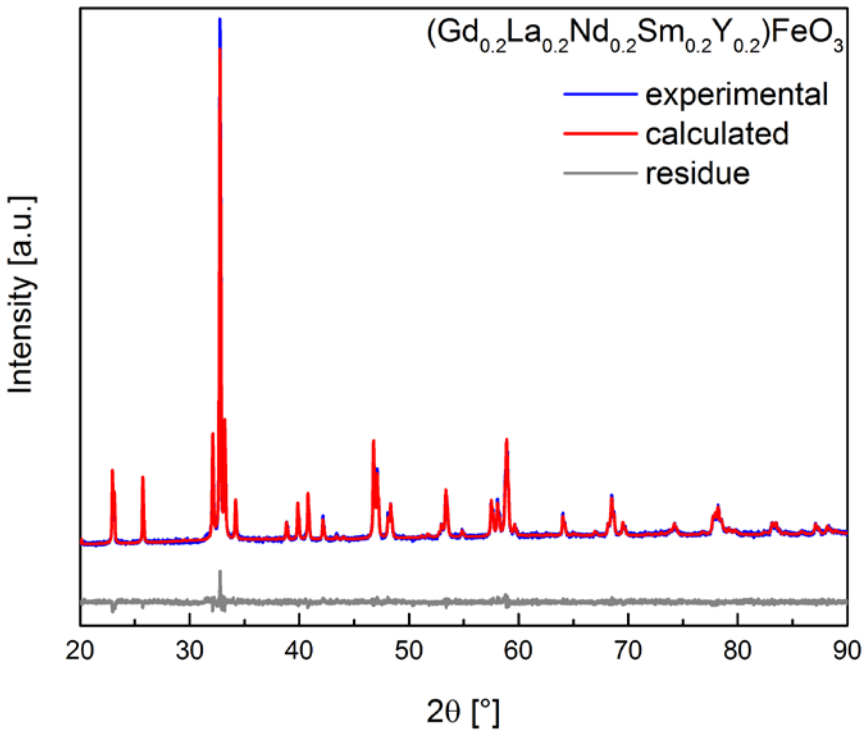


**Figure S4.** XRD pattern together with Rietveld fit of $(5A_{0.2})FeO_3$, confirming the presence of a single perovskite (*Pbnm*) phase.

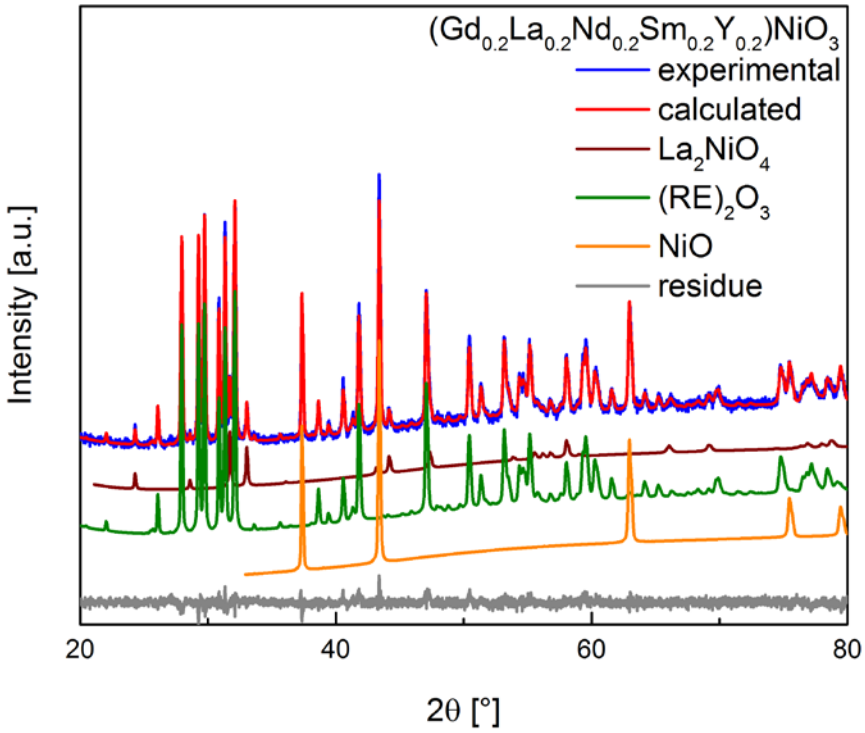


**Figure S5.** XRD pattern together with Rietveld fit of $(5A_{0.2})NiO_3$, where three different phases, tetragonal, monoclinic and rocksalt, are observed.

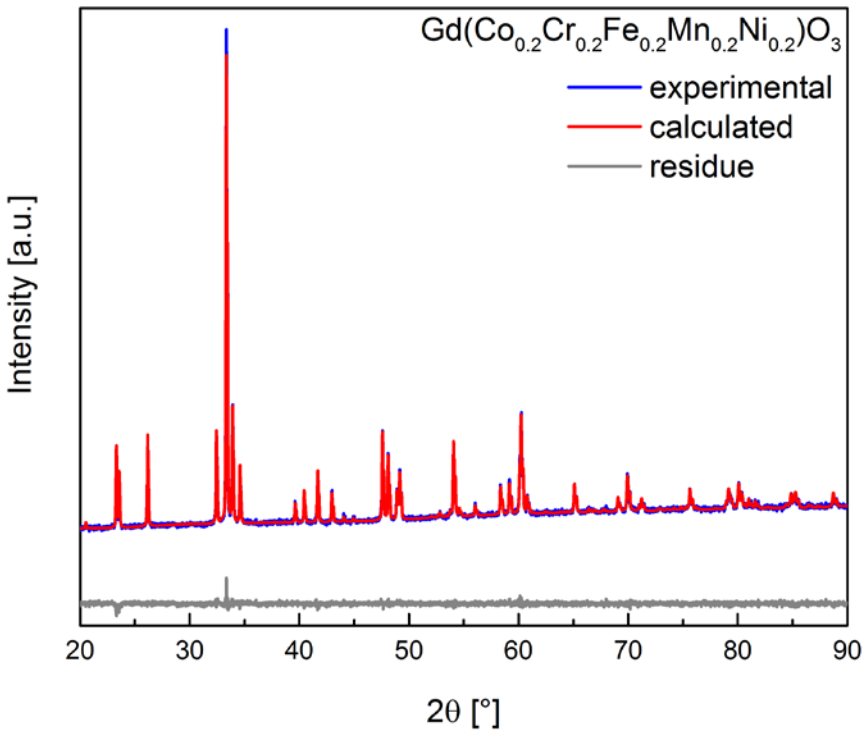


**Figure S6.** XRD pattern together with Rietveld fit of $Gd(5B_{0.2})O_3$, confirming the presence of a single perovskite (*Pbnm*) phase.

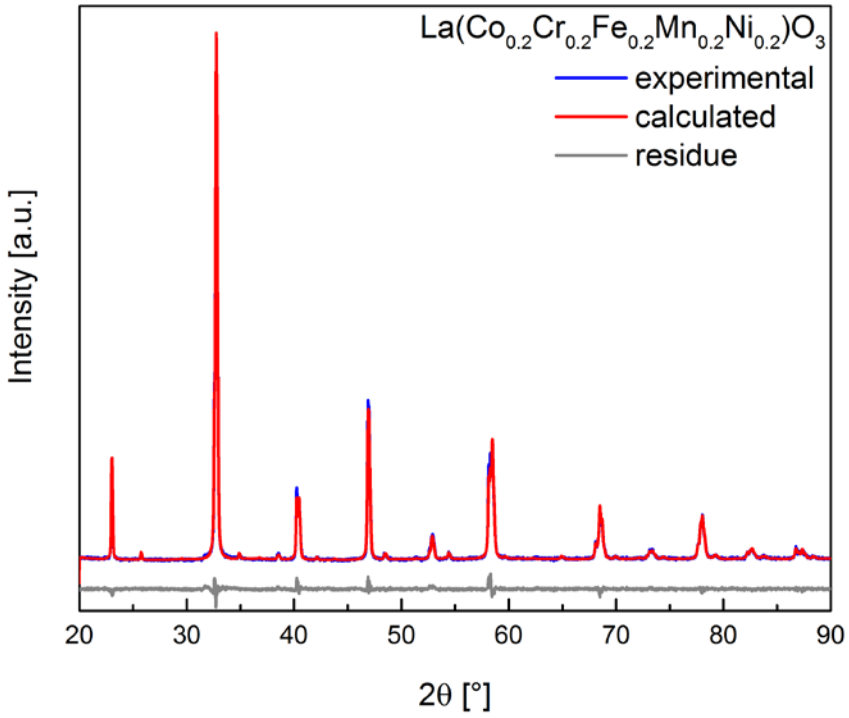


**Figure S7.** XRD pattern together with Rietveld fit of $La(5B_{0.2})O_3$, confirming the presence of a single perovskite (*Pbnm*) phase

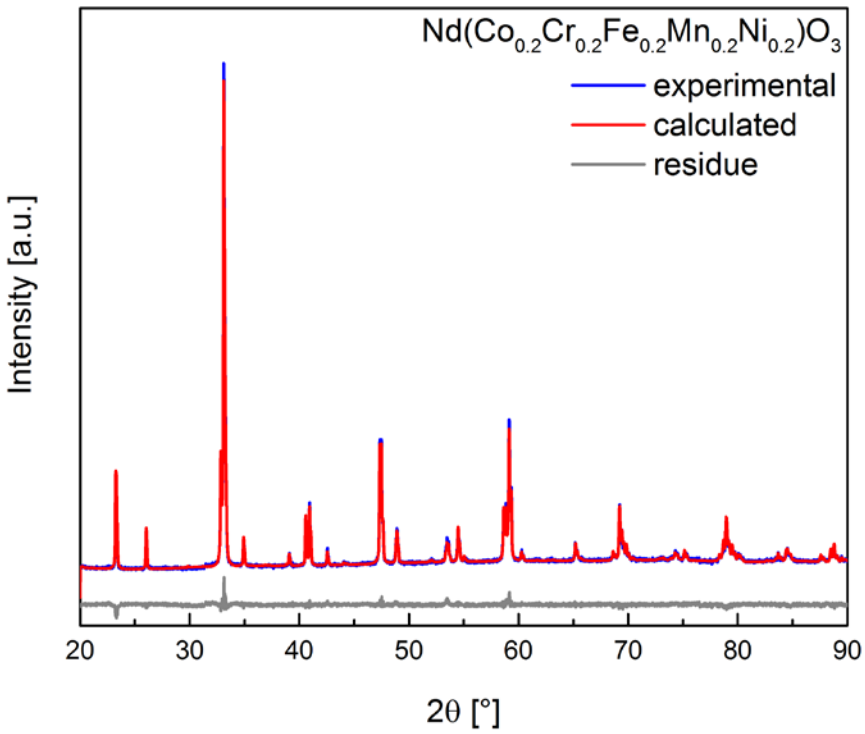


**Figure S8.** XRD pattern together with Rietveld fit of $Nd(5B_{0.2})O_3$, confirming the presence of a single perovskite (*Pbnm*) phase.

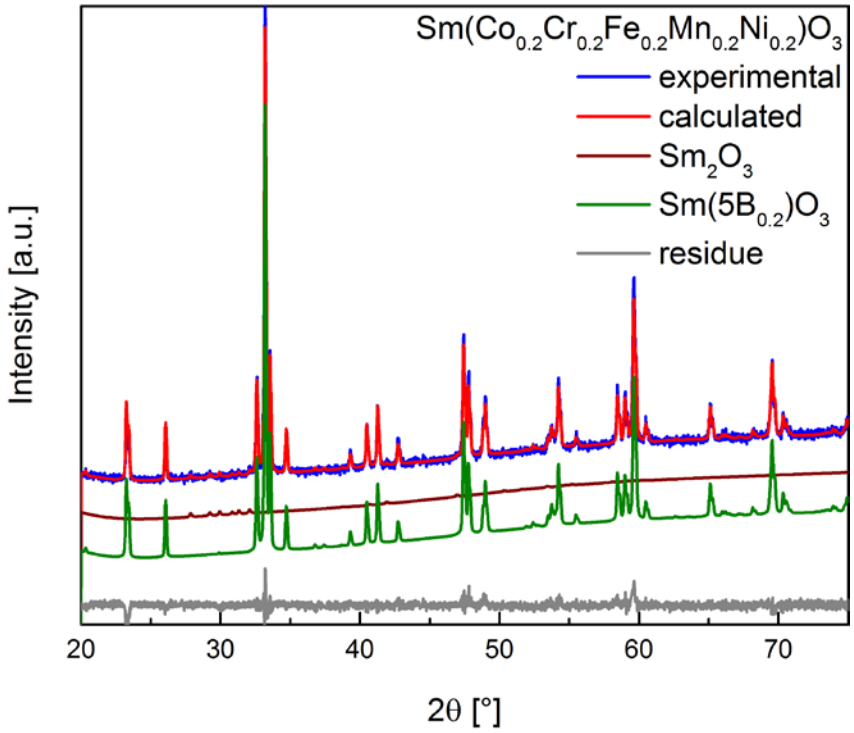


**Figure S9.** XRD pattern together with Rietveld fit of $Sm(5B_{0.2})O_3$, where small amount of secondary $Sm_2O_3$ phase alongside the major perovskite phase was observed.

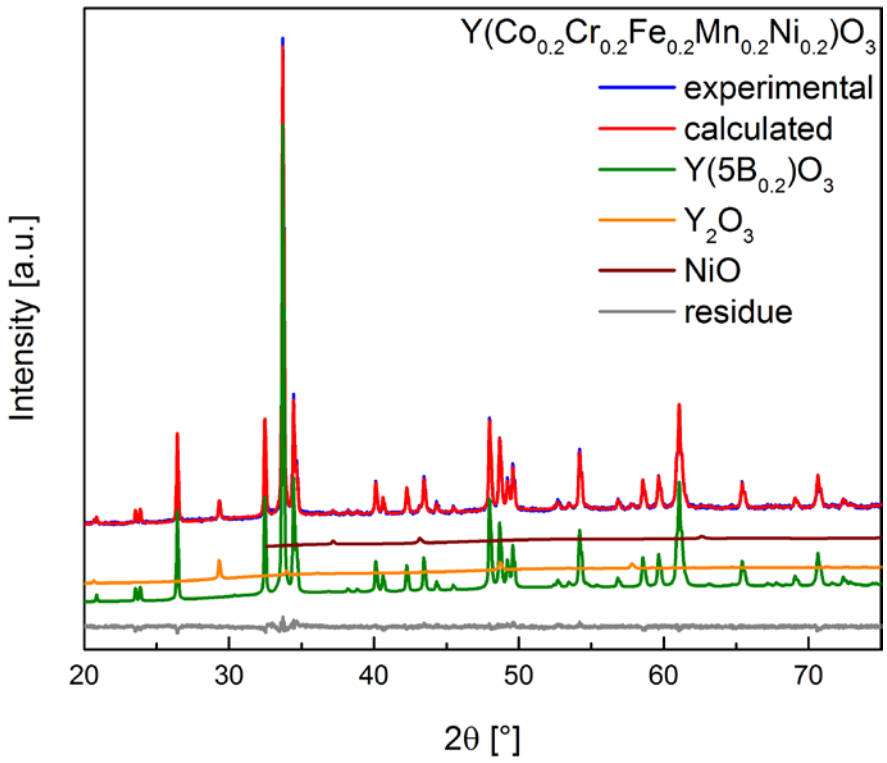


**Figure S10.** XRD pattern together with Rietveld fit of $Y(5B_{0.2})O_3$, where two secondary phases ($Y_2O_3$ and NiO) alongside the major perovskite phase was observed.

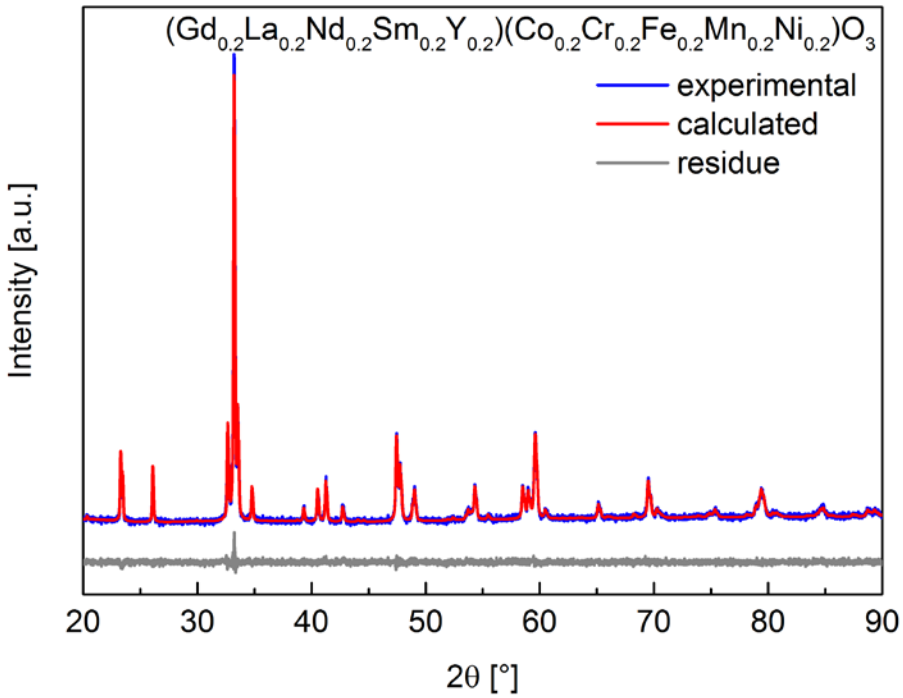


**Figure S11.** XRD pattern together with Rietveld fit of $(5A_{0.2})(5B_{0.2})O_3$, confirming the phase purity (*Pbmn*) of the highly complex 10 cationic system.

**Table S6.** Structural data for 8 phase perovskite mixtures observed in $(5A_{0.2})MnO_3$ system obtained from Rietveld refinement: space group (SG) along with prototype structures of secondary phases, phase fraction (*f* in wt.%) and lattice parameters (*a*, *b*, *c* in Å).

| SG | *f* | *a* | *b* | *c* |
|---|---|---|---|---|
| ***Pbnm*** | 25.6(1) | 5.3658(4) | 5.7521(4) | 7.5250(5) |
| ***Pbnm*** | 25.2(1) | 5.3661(9) | 5.7697(9) | 7.5136(1) |
| ***Pbnm*** | 25.1(5) | 5.3656(2) | 5.7345(2) | 7.5364(3) |
| ***Pbnm*** | 7.8(1) | 5.3654(1) | 5.7169(2) | 7.5478(2) |
| ***Pbnm*** | 7.7(2) | 5.3651(2) | 5.6993(3) | 7.5593(3) |
| ***Pbnm*** | 3.0(1) | 5.3649(5) | 5.6817(6) | 7.5707(5) |
| ***Pbnm*** | 2.8(1) | 5.3647(1) | 5.6641(6) | 7.5821(8) |
| ***Pbnm*** | 2.8(1) | 5.3644(8) | 5.6465(6) | 7.5936(1) |

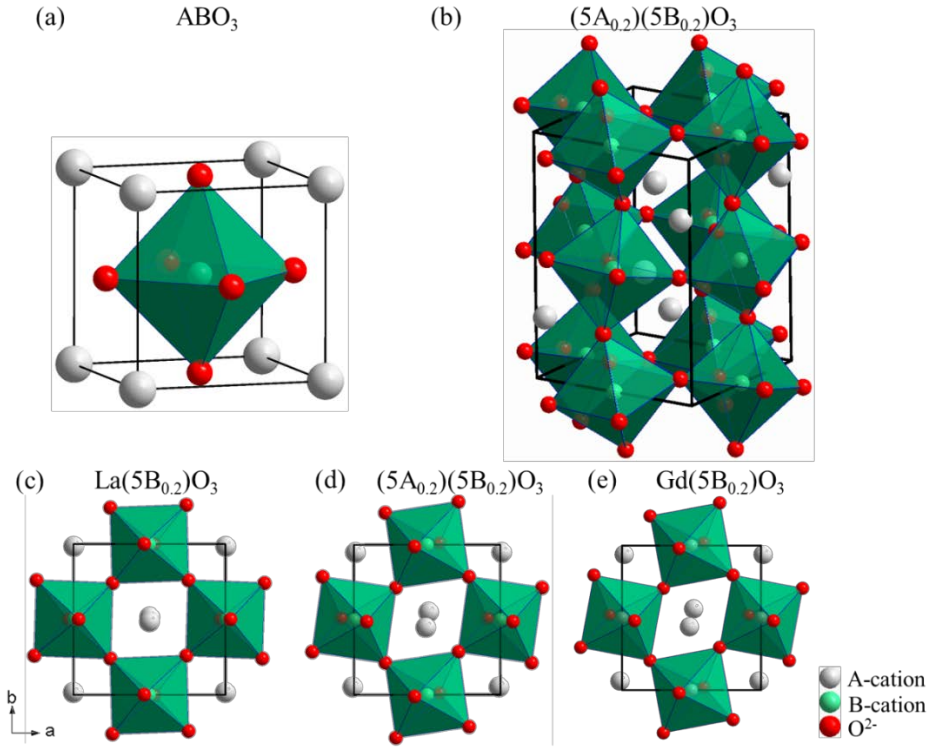


**Figure S12.** Schematic of crystal structure of an ideal cubic perovskite, $ABO_3$ ($Pm\bar{3}m$) (a) and $(5A_{0.2})(5B_{0.2})O_3$ (b) as a representative orthorhombic (*Pbnm*) ME-PO systems. The increasing magnitude of tilting the $BO_6$ polyhedra observed in ME-POs along [001] axis in: $La(5B_{0.2})O_3$ (c), $(5A_{0.2})(5B_{0.2})O_3$ (d), and $Gd(5B_{0.2})O_3$ (e).

**Table S7.** M-O bond distances (error ~ 0.01Å) for different ME-POs obtained from Rietveld analysis the corresponding XRD patterns.

| **$(5A_{0.2})CoO_3$** | | **$(5A_{0.2})CrO_3$** | | **$(5A_{0.2})FeO_3$** | | **$(5A_{0.2})MnO_3$** | | **$Gd(5B_{0.2})O_3$** | | **$La(5B_{0.2})O_3$** | | **$Nd(5B_{0.2})O_3$** | | **$Sm(5B_{0.2})O_3$** | | **$Y(5B_{0.2})O_3$** | | **$(5A_{0.2})(5B_{0.2})O_3$** | |
|---|---|---|---|---|---|---|---|---|---|---|---|---|---|---|---|---|---|---|---|
| **A-O distances** | | | | | | | | | | | | | | | | | | | |
| **O1** | 2.29 | O1 | 2.32 | O1 | 2.35 | O1 | 2.21 | O1 | 2.30 | O2 | 2.57 | O1 | 2.29 | O1 | 2.38 | O1 | 2.22 | O1 | 2.35 |
| **O2** | 2.34 | O2 | 2.40 | O2 | 2.39 | O2 | 2.47 | O1 | 2.37 | O2 | 2.57 | O2 | 2.44 | O1 | 2.44 | O2 | 2.27 | O2 | 2.43 |
| **O2** | 2.34 | O2 | 2.40 | O2 | 2.39 | O2 | 2.47 | O2 | 2.43 | O1 | 2.57 | O2 | 2.44 | O2 | 2.48 | O2 | 2.27 | O2 | 2.43 |
| **O1** | 2.43 | O1 | 2.47 | O1 | 2.43 | O2 | 2.53 | O2 | 2.43 | O2 | 2.57 | O1 | 2.49 | O2 | 2.48 | O1 | 2.30 | O1 | 2.46 |
| **O2** | 2.54 | O2 | 2.58 | O2 | 2.59 | O2 | 2.53 | O2 | 2.58 | O2 | 2.57 | O2 | 2.55 | O2 | 2.59 | O2 | 2.48 | O2 | 2.51 |
| **O2** | 2.54 | O2 | 2.58 | O2 | 2.59 | O2 | 2.64 | O2 | 2.58 | O1 | 2.66 | O2 | 2.55 | O2 | 2.59 | O2 | 2.48 | O2 | 2.51 |
| **O2** | 2.61 | O2 | 2.66 | O2 | 2.69 | O2 | 2.64 | O2 | 2.59 | O1 | 2.82 | O2 | 2.73 | O2 | 2.62 | O2 | 2.63 | O2 | 2.70 |
| **O2** | 2.61 | O2 | 2.66 | O2 | 2.69 | O1 | 2.68 | O2 | 2.59 | O2 | 2.84 | O2 | 2.73 | O2 | 2.62 | O2 | 2.63 | O2 | 2.70 |
| **O1** | 3.02 | O1 | 3.09 | O1 | 3.11 | O1 | 3.26 | O1 | 3.07 | O2 | 2.84 | O1 | 3.14 | O1 | 3.06 | O1 | 3.12 | O1 | 3.11 |
| **O1** | 3.02 | O1 | 3.12 | O1 | 3.26 | O1 | 3.43 | O1 | 3.32 | O1 | 2.94 | O1 | 3.17 | O1 | 3.15 | O1 | 3.14 | O1 | 3.14 |
| **O2** | 3.05 | O2 | 3.31 | O2 | 3.42 | O2 | 3.43 | O2 | 3.33 | O2 | 3.01 | O2 | 3.29 | O2 | 3.25 | O2 | 3.51 | O2 | 3.32 |
| **O2** | 3.05 | O2 | 3.31 | O2 | 3.42 | O2 | 2.21 | O2 | 3.33 | O2 | 3.01 | O2 | 2.29 | O2 | 3.25 | O2 | 3.51 | O2 | 3.32 |
| **B-O distances** | | | | | | | | | | | | | | | | | | | |
| **O2** | 1.92 | O2 | 1.97 | O1 | 1.98 | O1 | 1.98 | O1 | 1.95 | O1 | 1.94 | O2 | 1.95 | O2 | 1.94 | O1 | 1.96 | O2 | 1.95 |
| **O2** | 1.92 | O2 | 1.97 | O1 | 1.98 | O1 | 1.98 | O1 | 1.95 | O1 | 1.94 | O2 | 1.95 | O2 | 1.94 | O1 | 1.96 | O2 | 1.95 |
| **O1** | 1.93 | O1 | 1.97 | O2 | 1.99 | O2 | 1.96 | O2 | 1.96 | O2 | 1.94 | O1 | 1.99 | O1 | 1.95 | O2 | 1.98 | O1 | 1.96 |
| **O1** | 1.93 | O1 | 1.97 | O2 | 1.99 | O2 | 1.96 | O2 | 1.96 | O2 | 1.94 | O1 | 1.99 | O1 | 1.95 | O2 | 1.98 | O1 | 1.96 |
| **O2** | 1.93 | O2 | 1.98 | O2 | 2.02 | O2 | 2.14 | O2 | 1.99 | O2 | 1.96 | O2 | 2.00 | O2 | 1.98 | O2 | 1.99 | O2 | 1.98 |
| **O2** | 1.93 | O2 | 1.98 | O2 | 2.02 | O2 | 2.14 | O2 | 1.99 | O2 | 1.96 | O2 | 2.00 | O2 | 1.98 | O2 | 1.99 | O2 | 1.98 |

$5A_{0.2}$ = $Gd_{0.2}La_{0.2}Nd_{0.2}Sm_{0.2}Y_{0.2}$, $5B_{0.2}$ = $Co_{0.2}Cr_{0.2}Fe_{0.2}Mn_{0.2}Ni_{0.2}$

**Effective coordination number (ECoN)**

The effective coordination number (ECoN) for the cations are calculated based on the formulation proposed by Hoppe:[3]

$$ECoN = \sum_{i=1}^{n} e^{\left[1-\left\{\frac{(f_{MO})_i}{f_{MFIR}}\right\}^6\right]} \quad \text{(S1)}$$

where $f_{MO}$ and $f_{MFIR}$ are the fictive and the mean fictive ionic radii, respectively, and are calculated as follows:

$$f_{MO} = (M \rightarrow O) \cdot \left[\frac{r_M}{r_M + r_O}\right] \quad \text{(S1)}$$

$$f_{MFIR} = \frac{\sum_{i=1}^{n}(f_{MO})_i \cdot e^{\left[1-\left\{\frac{(f_{MO})_i}{(f_{MO})_{i=1}}\right\}^6\right]}}{\sum_{i=1}^{n} e^{\left[1-\left\{\frac{(f_{MO})_i}{(f_{MO})_{i=1}}\right\}^6\right]}} \quad \text{(S2)}$$

where $(M \rightarrow O)$ stands for the bond distance between a cation and a neighboring oxygen ion (see Table S7), $r_M$ and $r_O$ are the cation and oxygen ion radii, respectively (see Table S1). The value of *n* should be theoretically infinite. However, due to negligible contribution of the far off ions *n* is fixed to 12 for calculation of the ECoN(A) and to 6 for calculation of the ECoN(B).

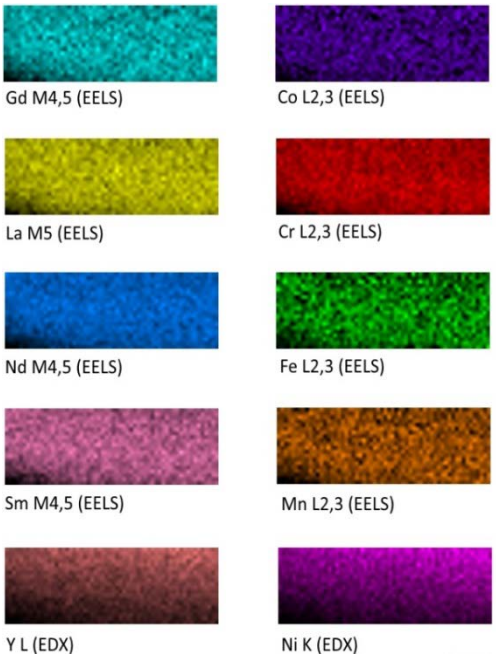


**Figure S13.** EELS and EDX elemental maps showing homogenous distribution of elements in $(5A_{0.2})(5B_{0.2})O_3$.

**Table S8.** Structural data for the $(5A_{0.2})MnO_3$ systems at different temperatures (T) obtained from Rietveld refinement: space group (SG), phase fraction (*f* in wt.%) and lattice parameters (*a*, *b*, *c* in Å).

| T [°C] | SG | *f* | *a* | *b* | *c* |
|---|---|---|---|---|---|
| **30 (before HTXRD)** | *Pbnm* | 42.3(1) | 5.3658(4) | 5.7396(4) | 7.5352(5) |
| | *Pbnm* | 40.9(1) | 5.3670(9) | 5.7637(9) | 7.5201(1) |
| | *Pbnm* | 16.8(5) | 5.3633(2) | 5.6916(2) | 7.5652(3) |
| **400** | *Pbnm* | 81.4(4) | 5.3927(2) | 5.6662(2) | 7.6216(3) |
| | *Pbnm* | 17.5(4) | 5.3888(7) | 5.6287(5) | 7.6616(8) |
| | *Pbnm* | 1.1(9) | 5.3240(5) | 5.8440(5) | 7.9560(6) |
| **500** | *Pbnm* | 86.4(4) | 5.4011(2) | 5.6488(2) | 7.6487(2) |
| | *Pbnm* | 13.6(4) | 5.3978(8) | 5.6129(5) | 7.6887(9) |
| **600** | *Pbnm* | 93.0(4) | 5.4111(2) | 5.6260(2) | 7.6778(2) |
| | *Pbnm* | 7.0(4) | 5.4093(1) | 5.5945(9) | 7.7188(1) |
| **700** | *Pbnm* | 97.4(3) | 5.4214(1) | 5.5992(1) | 7.7040(1) |
| | *Pbnm* | 2.6(3) | 5.4170(3) | 5.6800(2) | 7.7440(3) |
| **800** | *Pbnm* | 98.3(3) | 5.4340(7) | 5.6016(8) | 7.7255(1) |
| | *Pbnm* | 1.7(3) | 5.4470(2) | 5.5731(1) | 7.7660(9) |
| **900** | *Pbnm* | 100 | 5.4450(6) | 5.6046(7) | 5.7435(1) |
| **1000** | *Pbnm* | 100 | 5.4611(7) | 5.6037(7) | 7.7680(1) |
| **30 (after HTXRD)** | *Pbnm* | 37.2(1) | 5.3656(4) | 5.7449(8) | 7.5317(7) |
| | *Pbnm* | 31.7(2) | 5.3657(9) | 5.7678(9) | 7.5191(1) |
| | *Pbnm* | 31.1(8) | 5.3654(1) | 5.7220(2) | 7.5444(2) |

**High Temperature X-Ray Diffraction (HT-XRD)**

The structural parameters obtained from the Rietveld analysis for the $(5A_{0.2})(5B_{0.2})O_3$ systems, at different temperatures, are summarized in Table S8. It was observed that the orthorhombic distortion in the ME-POs was maintained even at higher temperatures (till 1000 $^oC$). However, linear expansion of the lattice parameters and a decrease in the metric distortion form the cubic structure was observed with increasing the temperature.

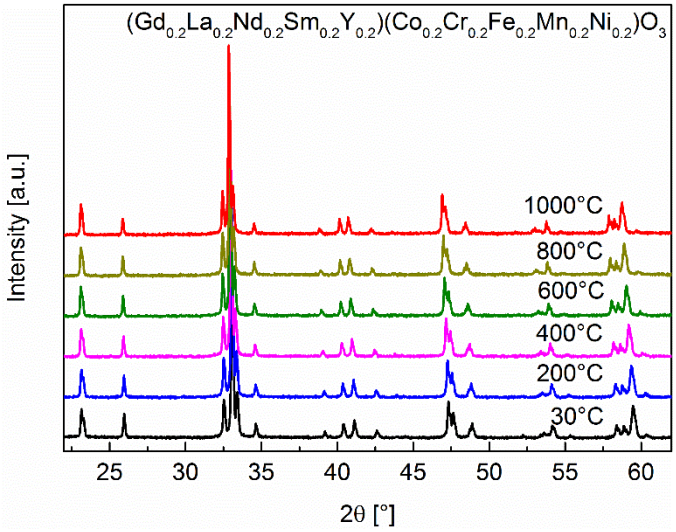


**Figure S14:** In situ HT-XRD patterns of $(5A_{0.2})(5B_{0.2})O_3$ at different temperatures indicating no phase separation or change in the lattice symmetry.

**Table S9.** Structural data for the 10 cationic $(5A_{0.2})(5B_{0.2})O_3$ systems at different temperatures (T) obtained from Rietveld refinement: space group (SG), phase fraction ($f$ in wt.%), lattice parameters ($a$, $b$, $c$, $a_{ps.cubic}$ in Å), and degree of metric distortion ($\varepsilon$ in %).

| T [°C] | SG | *f* | *a* | *b* | *c* | $a_{ps.cubic}$ | $\varepsilon$ |
|---|---|---|---|---|---|---|---|
| **30** | *Pbnm* | 100 | 5.3614(7) | 5.5012(7) | 7.6309(1) | 3.832 | 0.63 |
| **200** | *Pbnm* | 100 | 5.3738(5) | 5.5087(4) | 7.6478(9) | 3.839 | 0.61 |
| **400** | *Pbnm* | 100 | 5.3915(6) | 5.5219(5) | 7.6717(9) | 3.850 | 0.58 |
| **600** | *Pbnm* | 100 | 5.4097(5) | 5.5361(5) | 7.6972(1) | 3.862 | 0.56 |
| **800** | *Pbnm* | 100 | 5.4280(3) | 5.5483(4) | 7.7216(2) | 3.874 | 0.53 |
| **1000** | *Pbnm* | 100 | 5.4454(4) | 5.5579(1) | 7.7444(3) | 3.884 | 0.50 |

$a_{ps.cubic}$ is the pseudo-cubic lattice parameter calculated using Eq. 4.

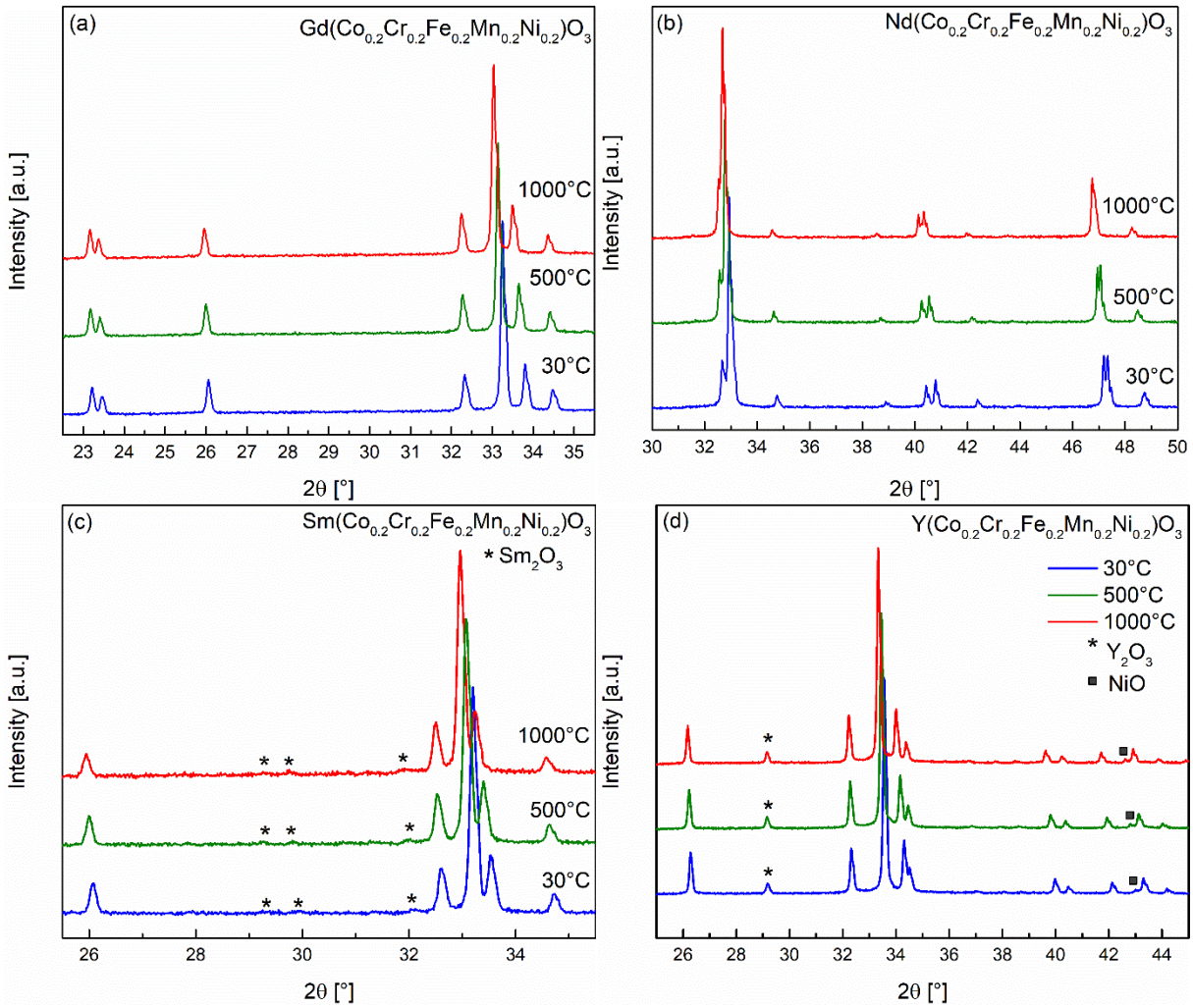


**Figure S15.** In situ HT-XRD pattern (at 30 °C, 500 °C and 1000 °C) of the different ME-PO systems with multiple cations on the B site where (a) $Gd(Co_{0.2}Cr_{0.2}Fe_{0.2}Mn_{0.2}Ni_{0.2})O_3$; (b) $Nd(Co_{0.2}Cr_{0.2}Fe_{0.2}Mn_{0.2}Ni_{0.2})O_3$; (c) $Sm(Co_{0.2}Cr_{0.2}Fe_{0.2}Mn_{0.2}Ni_{0.2})O_3$ and (d) $Y(Co_{0.2}Cr_{0.2}Fe_{0.2}Mn_{0.2}Ni_{0.2})O_3$. No changes other than lattice expansion at higher temperatures were observed in the systems.

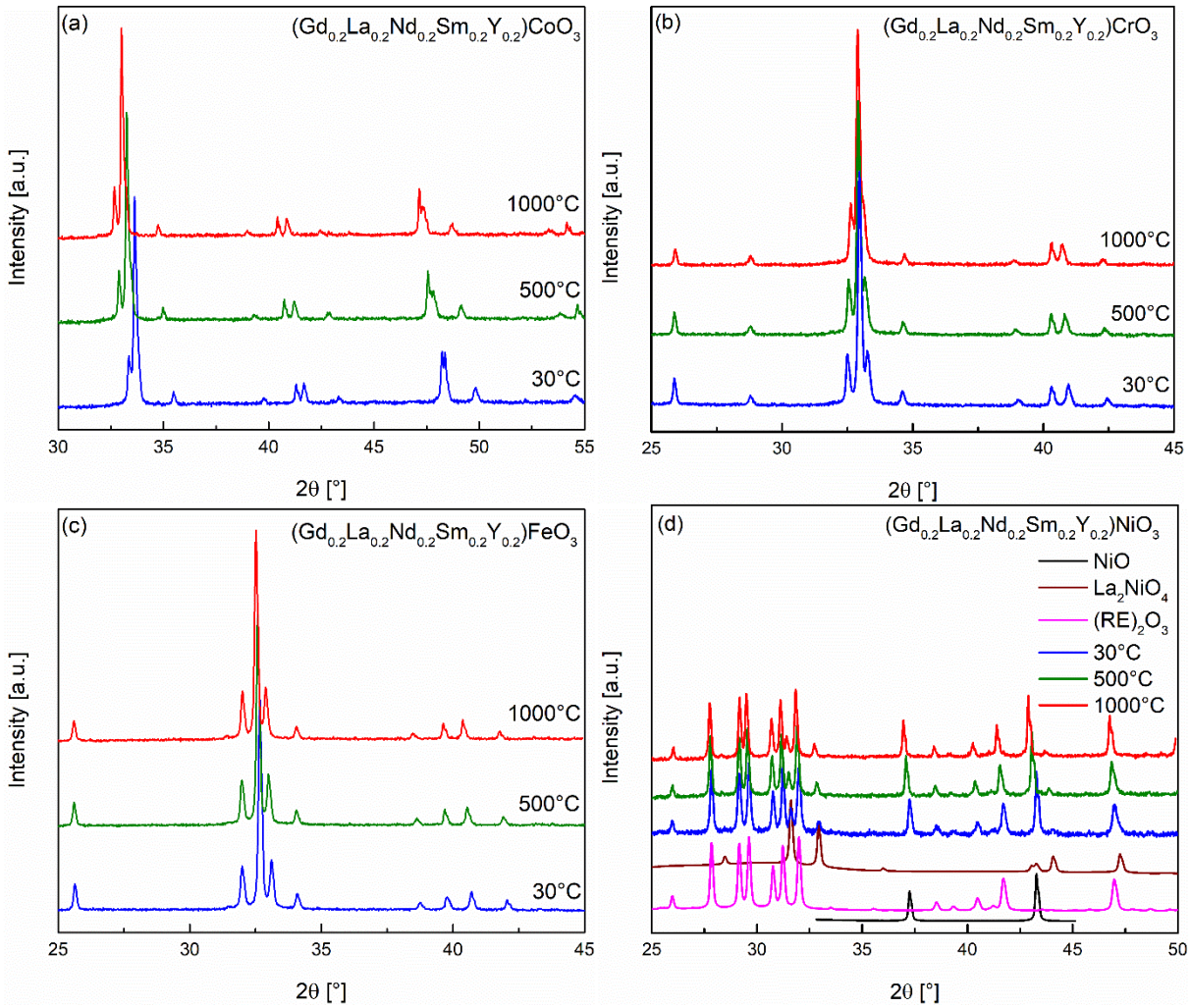


**Figure S16.** In situ HT-XRD pattern (at 30 °C, 500 °C and 1000 °C) of the different ME-PO systems with multiple cations on the A site where (a) $(Gd_{0.2}La_{0.2}Nd_{0.2}Sm_{0.2}Y_{0.2})CoO_3$; (b) $(Gd_{0.2}La_{0.2}Nd_{0.2}Sm_{0.2}Y_{0.2})CrO_3$; (c) $(Gd_{0.2}La_{0.2}Nd_{0.2}Sm_{0.2}Y_{0.2})FeO_3$ and (d) $(Gd_{0.2}La_{0.2}Nd_{0.2}Sm_{0.2}Y_{0.2})NiO_3$. No changes other than lattice expansion at higher temperatures were observed in the systems.

**Table S10.** Structural data for the La($5B_{0.2}$)$O_3$ systems at different temperatures (T) obtained from Rietveld refinement: space group (SG), phase fraction (*f* in wt.%), lattice parameters (*a*, *b*, *c* in Å) and metric strain ($\varepsilon$).

| T [°C] | SG | *f* | *a* | *b* | *c* | $\varepsilon$ [%] |
|---|---|---|---|---|---|---|
| **30 (before HTXRD)** | *Pbnm* | 100 | 5.4656(6) | 5.5101(5) | 7.7424(9) | 0.198 |
| **100** | *Pbnm* | 100 | 5.4687(1) | 5.5152(1) | 7.7480(1) | 0.214 |
| **125** | *Pbnm* | 84.6(4) | 5.4994(1) | 5.5166(1) | 7.7517(2) | 0.223 |
| | $R\bar{3}ch$ | 15.4(4) | 5.5161(3) | - | 13.2842(1) | 0.460 |
| **140** | *Pbnm* | 39.5(4) | 5.4707(1) | 5.5179(1) | 7.7536(2) | 0.223 |
| | $R\bar{3}ch$ | 60.5(4) | 5.5175(1) | - | 13.2863(4) | 0.463 |
| **150** | *Pbnm* | 19.2(3) | 5.4717(1) | 5.5189(2) | 7.7550(2) | 0.227 |
| | $R\bar{3}ch$ | 80.8(3) | 5.5180(1) | - | 13.2903(3) | 0.457 |
| **175** | *Pbnm* | 5.4(3) | 5.4721(5) | 5.5193(5) | 7.7556(7) | 0.228 |
| | $R\bar{3}ch$ | 94.6(3) | 5.5194(9) | - | 13.2966(3) | 0.451 |
| **300** | *Pbnm* | 3.2(3) | 5.4790(7) | 5.5263(7) | 7.7653(1) | 0.265 |
| | $R\bar{3}ch$ | 96.8(3) | 5.5272(1) | - | 13.3344(3) | 0.413 |
| **450** | $R\bar{3}ch$ | 100 | 5.5369(7) | - | 13.3799(2) | 0.368 |
| **600** | $R\bar{3}ch$ | 100 | 5.5474(5) | - | 13.4260(1) | 0.326 |
| **750** | $R\bar{3}ch$ | 100 | 5.5578(5) | - | 13.4699(1) | 0.288 |
| **900** | $R\bar{3}ch$ | 100 | 5.5675(5) | - | 13.5124(1) | 0.250 |
| **1050** | $R\bar{3}ch$ | 100 | 5.5767(4) | - | 13.5541(1) | 0.211 |
| **30 (after HTXRD)** | *Pbnm* | 100 | 5.4653(1) | 5.5106(9) | 7.7438(2) | 0.204 |

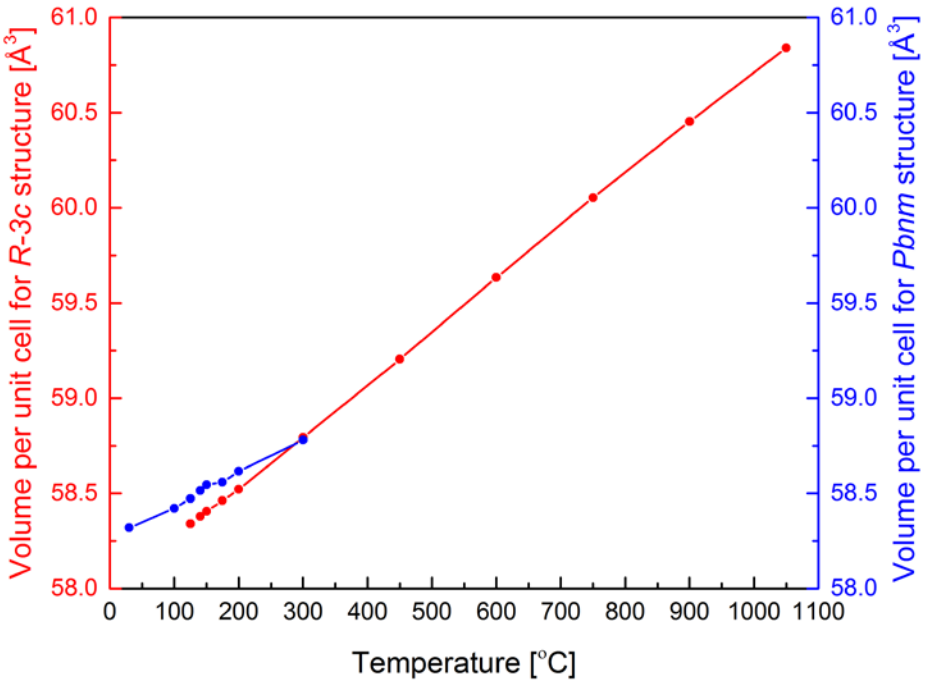


**Figure S17:** Volume change of the trigonal ($R\bar{3}ch$) and the orthorhombic (*Pbnm*) unit cell of $La(5B_{0.2})O_3$ system with increasing temperature.

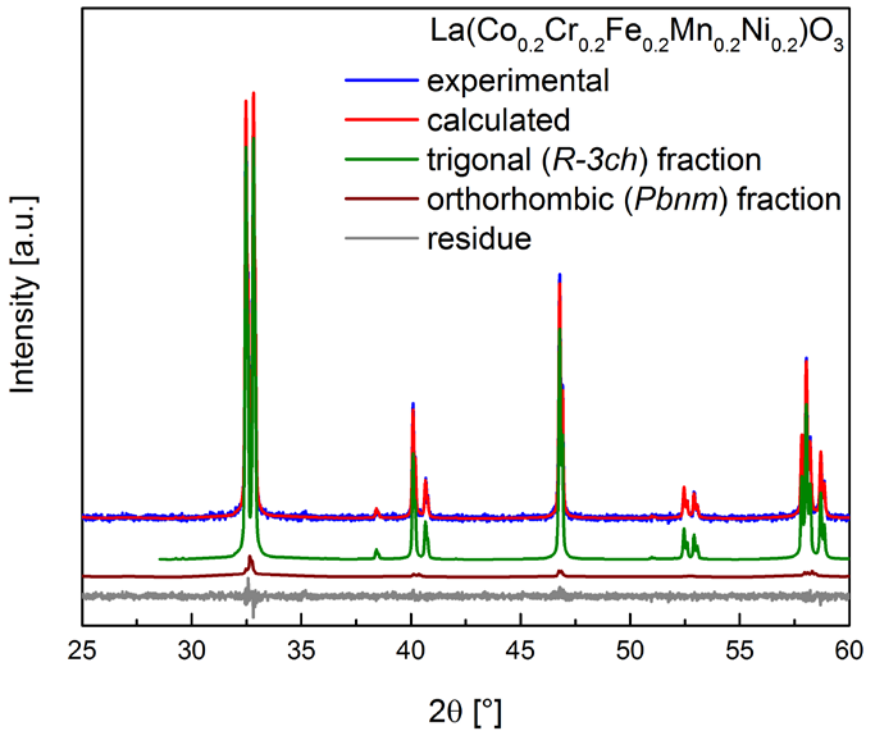


**Figure S18.** In-situ HTXRD pattern together with Rietveld fit of $La(5B_{0.2})O_3$ at 300 °C. A major (96.2 wt.%) trigonal phase along with a minor (3.8 wt.%) orthorhombic phase are adequately required to fit the pattern. Above this temperature only the trigonal phase is observed.

## References

(1) Shannon, R. D. Revised Effective Ionic Radii and Systematic Studies of Interatomic Distances in Halides and Chalcogenides. *Acta Crystallogr. Sect. A* **1976**, *32* (5), 751–767 DOI: 10.1107/S0567739476001551.

(2) Springer Materials (online database) http://materials.springer.com (accessed Mar 14, 2017).

(3) Hoppe, R. Effective Coordination Numbers (ECoN) and Mean Fictive Ionic Radii (MEFIR). *Zeitschrift für Krist.* **1979**, *150* (1–4), 23–52 DOI: 10.1524/zkri.1979.150.1-4.23.